Title

Telencephalic outputs from the medial entorhinal cortex are copied directly to the

hippocampus

Authors and Affiliations

Sau Yee Tsoi, Merve Öncül, Ella Svahn, Mark Robertson, Zuzanna Bogdanowicz, Christina

McClure and Gülşen Sürmeli*

*Corresponding Author

University of Edinburgh, Centre for Discovery Brain Sciences, Edinburgh, UK:

G.S., S.Y.T., M.Ö., E.S., M.R., Z.B., C.M.

Simons Initiative for the Developing Brain:

G.S.

Current addresses

University College London, UK:

E.S.

NHS Greater Glasgow and Clyde, UK:

M.R.

VectorBuilder Inc., 1010 W 35th Street, Suite 515 Chicago, IL 60609, USA:

C.M.

Abstract

Complementary actions of the neocortex and the hippocampus enable encoding and long-term storage of experience dependent memories. Standard models for memory storage assume that sensory signals reach the hippocampus from superficial layers of the entorhinal cortex (EC). Deep layers of the EC on the other hand relay hippocampal outputs to the telencephalic structures including many parts of the neocortex. Here we show that cells in Layer 5a of the medial EC send a copy of their telencephalic outputs back to the CA1 region of the hippocampus. Combining cell-type specific anatomical tracing, high-throughput RNA-sequencing based projection mapping and optogenetics aided circuit mapping, we show that these projections have a unique topography and target hippocampal pyramidal cells and interneurons. Our results suggest that rather than serving as a relay, deep EC may coordinate hippocampal-neocortical interactions in spatial cognition and memory.

Introduction

Interplay between the hippocampus and the neocortex is a central tenet of theories for systems memory consolidation (Marr, 1971; McClelland et al., 1995). The entorhinal cortex (EC) mediates the two-way communication between the neocortex and the hippocampus. Its superficial and deep layers respectively channel inputs to and outputs from the hippocampus. During a new experience the superficial layers relay convergent inputs from the cortex to the hippocampus where initial conjunctive representations of everyday experiences are generated. Subsequently during rest or sleep, hippocampal output is redistributed to the brain (Squire et al., 2015; Frankland and Bontempi 2005). Leading theoretical models consider the deep layers of EC as a relay of hippocampal output that reinstates neocortical activation patterns representing memories, enabling neocortex-wide synaptic changes required for long-term storage (Koster et al., 2018; Kumaran et al., 2016; McClelland et al., 1995; Schapiro et al., 2017).

Recent discoveries revealed complex and distinct input-output interactions of molecularly defined subtypes of neurons in the deep layers of medial EC (MEC), suggesting their functions extend beyond passing on hippocampal outputs. Layers 5a (L5a) and 5b (L5b) of the EC are genetically distinct with differential input-output organisations. L5a but not L5b is the sole origin of the long-range telencephalic outputs of the EC (Sürmeli et al., 2015), whereas L5b, but not L5a, is directly influenced by superficial layers of EC (Beed et al., 2020; Sürmeli et al., 2015). Inputs from the dorsal hippocampus preferentially target L5b over L5a (Rozov et al., 2020; Sürmeli et al., 2015; Wozny et al., 2018) whereas ventral hippocampus preferentially target L5a (Rozov et al. 2020). Moreover, the capacity of deep layers to integrate neocortical inputs with hippocampal output (Czajkowski et al. 2013; Beed et al. 2020; Sürmeli et al. 2015), suggest more complex roles.

78   An intriguing possibility, noted in experiments with classic retrograde tracers, is that deep

79   layers of MEC might also project to the hippocampal CA1 region, which provides the deep

80   EC with hippocampal output (Köhler, 1985; Witter and Amaral, 1991). Such recurrent

81   connectivity between CA1 and the deep MEC could be important in coordinating

82   hippocampal-entorhinal activity during memory consolidation (Ólafsdóttir et al. 2016),

83   provide a shortcut for hippocampal outputs to re-enter the hippocampus (Kumaran and

84   McClelland 2012) or have a more global coordination function encompassing the

85   hippocampus and the neocortex (Khodagholy et al., 2017). Despite its potential functional

86   significance, the key properties of this projection pathway including whether it shares the

87   same source with the telencephalon projections and which neurons it targets in the

88   hippocampus remain unknown.

89

90   Here we reveal that, neurons in L5a, but not L5b, of the MEC project to hippocampal CA1.

91   We establish that the telencephalon-projecting neurons copy their outputs directly to

92   pyramidal and subclasses of interneuron populations in CA1. Our results suggest that Layer

93   5a of the MEC has a dual function in coordinating neocortical and hippocampal networks.

94

95

96   **Results**

97   To find out whether neurons in either L5a or L5b project to the hippocampus we injected

98   retrograde adeno-associated viral vectors (AAVs) expressing green fluorescent protein

99   (GFP) or mCherry into intermediate hippocampus (Figure 1A,B; Figure 1- figure supplement

100   1A,B). As well as finding retrogradely-labelled cell bodies in layer 3 of MEC, which contains

101   neurons that are well-established as a critical input to stratum lacunosum/moleculare of CA1

102   (Naber et al., 2001; Kitamura et al., 2014), we also found labelled cell bodies in L5a, which

103   we identified by immunostaining against the ETS variant transcription factor-1 (Etv1) protein.

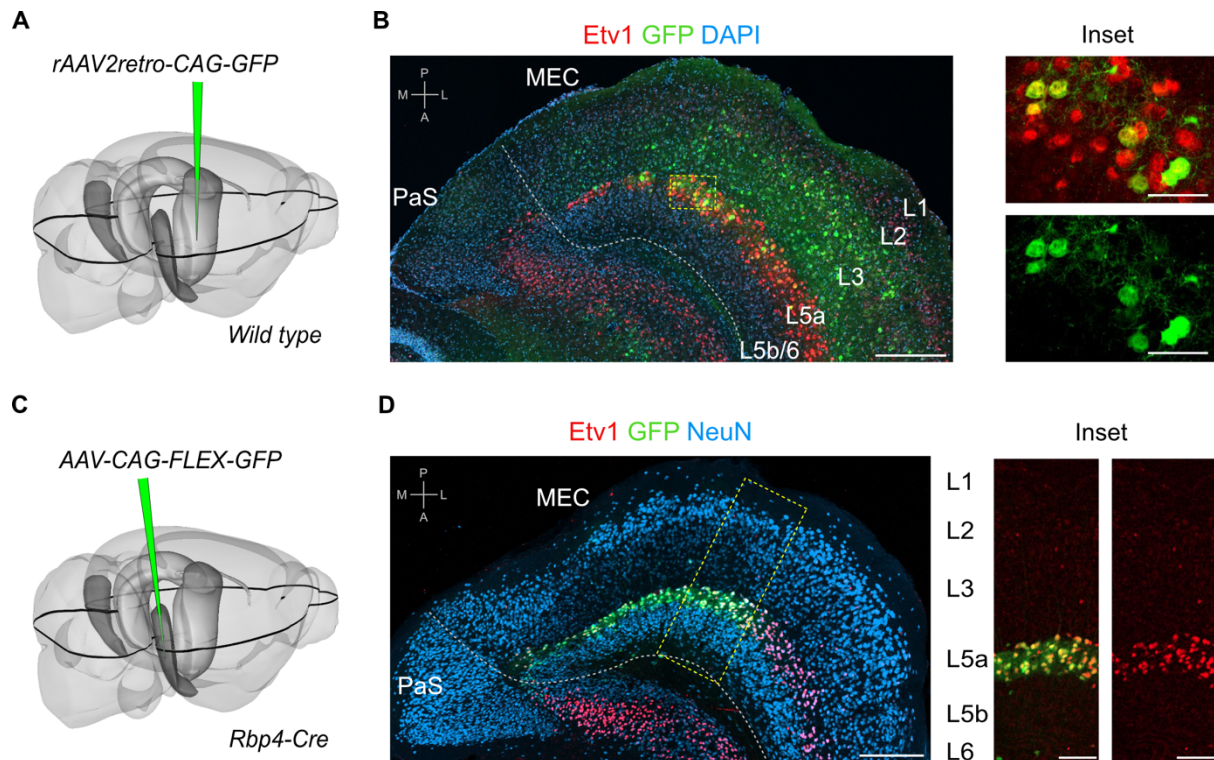104   Retrogradely-labelled neurons were not found in L5b.

Figure 1. L5a but not layer 5b of the MEC projects to the hippocampus

A, Schematic showing the injection site of a retrograde AAV in the intermediate hippocampus (light grey) of wild type mice. The black outline in the horizontal plane roughly corresponds to the dorso-ventral position of the horizontal section shown in B. Corresponding injection site image is shown in Figure 1- figure supplement 1A.

B, Immunostained brain section in the horizontal plane showing retrogradely-labelled neurons in L3 and L5a of the MEC. Etv1 expression marks L5a (Scale bar: 250 μm). Inset: high-magnification image of boxed region in left panel showing co-expression of GFP and Etv1 (Scale bar: 50 μm). Abbreviations: PaS, parasubiculum; P, posterior; A, anterior; M, medial; L, lateral.

C, Schematic showing the injection site of an AAV in the deep MEC (dark grey) of *Rbp4-Cre* mice for Cre dependent expression of GFP. The black outline in the horizontal plane roughly corresponds to the dorso-ventral position of the slice shown in D.

D, Entorhinal area on an immunostained brain section in the horizontal plane showing the overlapping expression of GFP with Etv1 (Scale bar: 250 μm). Inset: high-magnification of boxed region in middle panel showing GFP and Etv1 expression confined mainly to L5a in MEC (Scale bar: 100 μm).

105   To further investigate this projection, we identified and validated a transgenic mouse line that

106   enables specific genetic access to L5a. In this mouse line, Cre expression is driven by the

107   promoter of the retinol binding protein 4 gene (*Rbp4-Cre*; Gerfen et al., 2013). Following

108   injection of a Cre-dependent AAV expressing GFP or mCherry into the deep MEC of *Rbp4-*

109   *Cre* mice, fluorescent signal was detected mainly in L5a (Figure 1C,D and Figure 1- figure

110   supplement 1C). At the centre of the injection site, where labelling was densest, the majority

111   of neurons in L5a (71.3 ± 2.2 %, n = 3 mice, 180 neurons) were found to be fluorescently

112   labelled (Figure 1D). Labelled neurons were non-GABAergic (99.5 ± 0.3%, n = 3 mice, 1137

113   cells; Figure1- figure supplement 1D), most of which expressed Etv1 (88.6 ± 3.1 %, n = 3

114   mice, 1866 cells; Figure 1D). This is similar to the proportion of Etv1-expression in all L5a

115   neurons (Sürmeli et al., 2015) and also in retrogradely labelled subpopulations of L5a

116   neurons from the hippocampus and from cortical and subcortical target areas (Figure 1-

117   figure supplement 1E,F,G,H). Moreover, axons of L5a neurons labelled in the *Rbp4:Cre* line

118   were found in the telencephalon (Figure1-figure supplement 2). Thus, we established that

119   the *Rbp4-Cre* line provides unbiased genetic access to excitatory projection neurons in L5a.

120

121   To what extent does the projection from L5a to the hippocampus differ from previously-

122   identified projections arising from superficial layers of MEC? In contrast to projections from

123   superficial layers 2 and 3, which respectively target stratum lacunosum (SL) and stratum

124   moleculare (SM) of CA1 (Kitamura et al., 2014), axons from L5a neurons were primarily

125   found in deep stratum pyramidale (SP) and stratum lacunosum (SL), but were sparse in

126   stratum moleculare (SM; Figure 2A,B,C,D and Figure 2- figure supplement 1A). Axons from

127   L5a also differed in their proximo-distal organisation within CA1. Whereas projections from

128   superficial layers of MEC favour proximal CA1 (Tamamaki and Nojyo, 1995), axons from L5a

129   had highest density in distal CA1 (paired one-tailed Wilcoxon signed rank test, $p = 0.0312$, n

130   = 5 mice; Figure 2E,F,G,H and Figure 2- figure supplement 1B,C,D,E,F) and the subiculum

131   (Figure 2I and Figure 2- figure supplement 1G). We observed the same topography when

132   axons and axon terminals of L5a neurons were labelled with membrane-bound GFP and

133   fluorescently-tagged presynaptic proteins (synaptophysin), confirming that the topography is

134   not a result of labelling of passing axons (Figure 2J,K,L,M,N,O). This distinct topography

135   suggests a unique functional role for the projections from L5a of MEC to CA1.
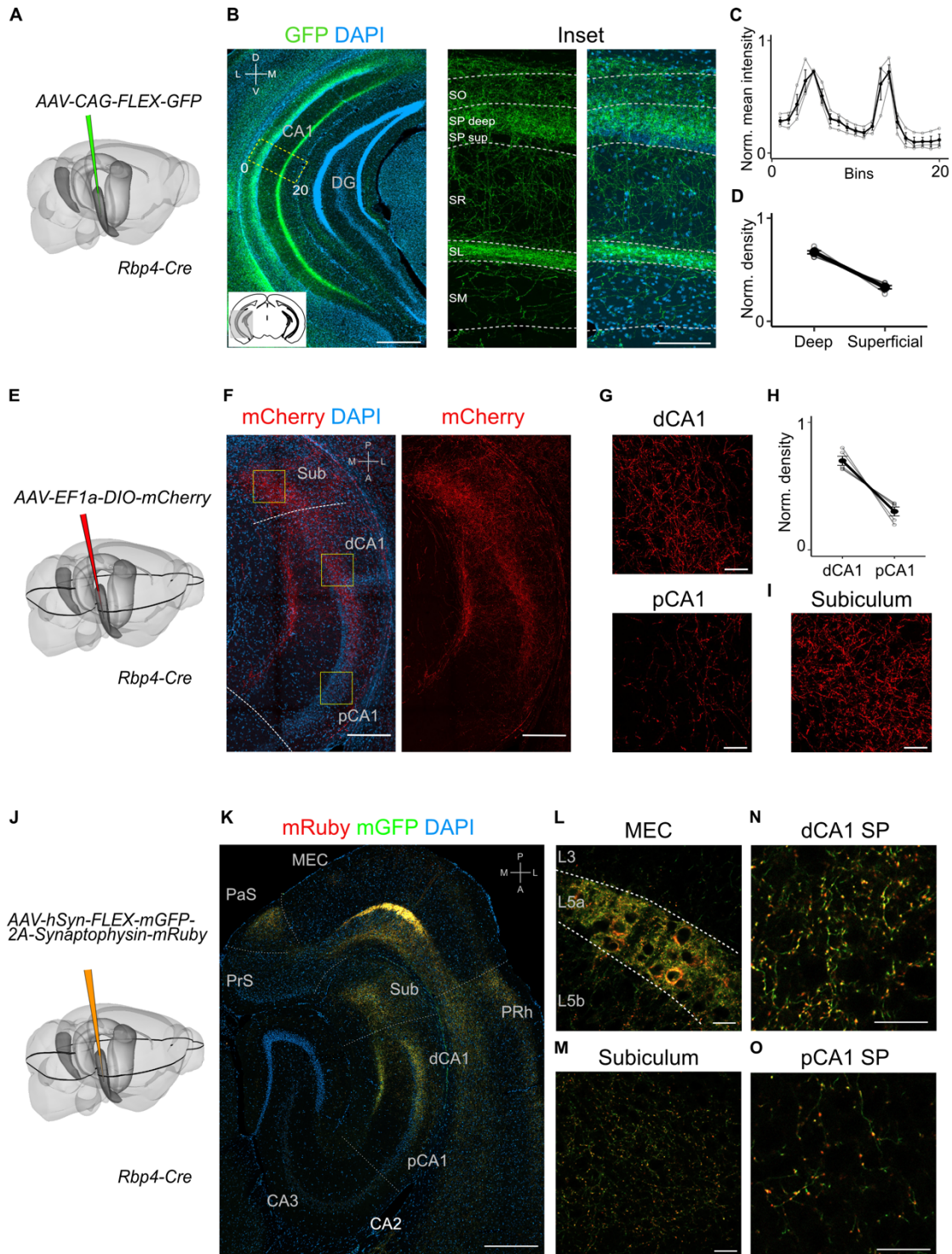
136

Figure 2. Projections to CA1 of L5a neurons of the MEC have distinct topography
A, Schematic showing the injection strategy of a Cre-dependent virus in the deep MEC of *Rbp4-Cre* mice.
B, Immunostained coronal brain section showing the distribution of axons of MEC L5a cells in CA1 (Scale bar: 500 µm). Inset: high-magnification image of boxed region in left panel (Scale bar: 100 µm). Bottom-left schematic indicates the antero-posterior position of the slice. Corresponding injection site image is shown in Figure 2- figure supplement 1A. Abbreviations: SO, stratum oriens; SP, stratum pyramidale; SR, stratum radiatum; SL, stratum lacunosum; SM, stratum moleculare; D, dorsal; V, ventral; M, medial; L, lateral.
C, Quantification of fluorescence intensity of GFP across the layers of CA1. The area between 0 and 20 in (B) was divided into 20 equally-sized bins, and the mean fluorescence intensity was calculated for each bin. Values shown are normalised mean fluorescence intensity values (n = 6 mice, 2 sections per brain).
D, Normalised mean fluorescence density values in deep versus superficial SP (n = 6 mice). Within SP, axon density in deep SP was significantly higher than density in superficial SP (paired one-tailed Wilcoxon signed rank test, p = 0.0156, n = 6).
E, Schematic showing the injection strategy of a Cre-dependent virus in the deep MEC of *Rbp4-Cre* mice. The black outline in the horizontal plane roughly corresponds to the dorso-ventral position of the horizontal slice shown in (F).
F, Immunostaining of a horizontal brain section showing the distribution of axons of MEC L5a cells in the subiculum (Sub), distal CA1 (dCA1) and proximal CA1 (pCA1; Scale bar: 200 µm). Corresponding injection site image is shown in Figure 2- figure supplement 1B.
G, High-magnification images of the pyramidal cell layer in distal (top) and proximal (bottom) CA1 showing axonal labelling (Scale bar: 20 µm).
H, Normalised mean fluorescence density values in distal versus proximal CA1 (n = 5 mice).
I, High-magnification image of the subiculum showing axonal labelling (Scale bar: 20 µm).
J, Schematic showing the injection strategy of an AAV for Cre-dependent expression of a membrane-bound form of GFP and a synaptophysin-mRuby conjugate in L5a of the MEC in the *Rbp4-Cre* mice. The black outline in the horizontal plane roughly corresponds to the dorso-ventral position of the slice shown in (K).
K, Immunostained brain section in the horizontal plane showing the distribution of axons (green) and synaptic terminals (red) in the hippocampus as well as the parasubiculum (PaS) and perirhinal cortex (PRh). Injection site in the MEC is distinguishable by the strong fluorescent labelling of L5a cell bodies (Scale bar: 400 µm).
L, High-magnification image of the injection site in the MEC showing cell membrane and synaptic labelling specifically in L5a (Scale bar: 20 µm).
M, High-magnification image of the subiculum showing axonal and synaptic labelling (Scale bar: 20 µm).
N,O, High-magnification images of the pyramidal cell layer in distal (N) and proximal (O) CA1 showing axonal and synaptic labelling (Scale bar: 20 µm).

137   Our findings suggest two intriguing possibilities for the organisation of output neurons in L5a

138   of the MEC. The hippocampus-projecting neurons in L5a may be distinct from the

139   telencephalon-projecting neurons, implying separate processing within the deep MEC layers

140   of signals to the hippocampus and telencephalon. Alternatively, the same neurons in L5a

141   may project to both the telencephalon and the hippocampus, implying that telencephalic

142   outputs from MEC are copied back to the hippocampus. To distinguish between these

143   possibilities we used a combinatorial viral labelling strategy. We restricted reporter gene

144   expression to subpopulations of L5a cells that project to specific targets by injecting a

145   retrograde AAV expressing Cre recombinase in either the retrosplenial cortex (RSC) or

146

147   nucleus accumbens (NucAcb), and a Cre-dependent fluorescent reporter virus into the MEC

148   (Figure 3A,B and Figure 3- figure supplement 1). With this approach we detected in CA1

149   fluorescently-labelled axons originating from both RSC-projecting and NucAcb-projecting

150   L5a neurons (Figure 3C,D). The axon distribution across layers was similar to when L5a

151   neurons were labelled in bulk using the *Rbp4-Cre* mouse line (Figure 3E,F). These results

152   establish the principle that axon projections from L5a of MEC to the hippocampus are

153   collaterals of projections to telencephalic targets. However, it is unclear from these

154   experiments whether this principle applies to projections from L5a to all of its many
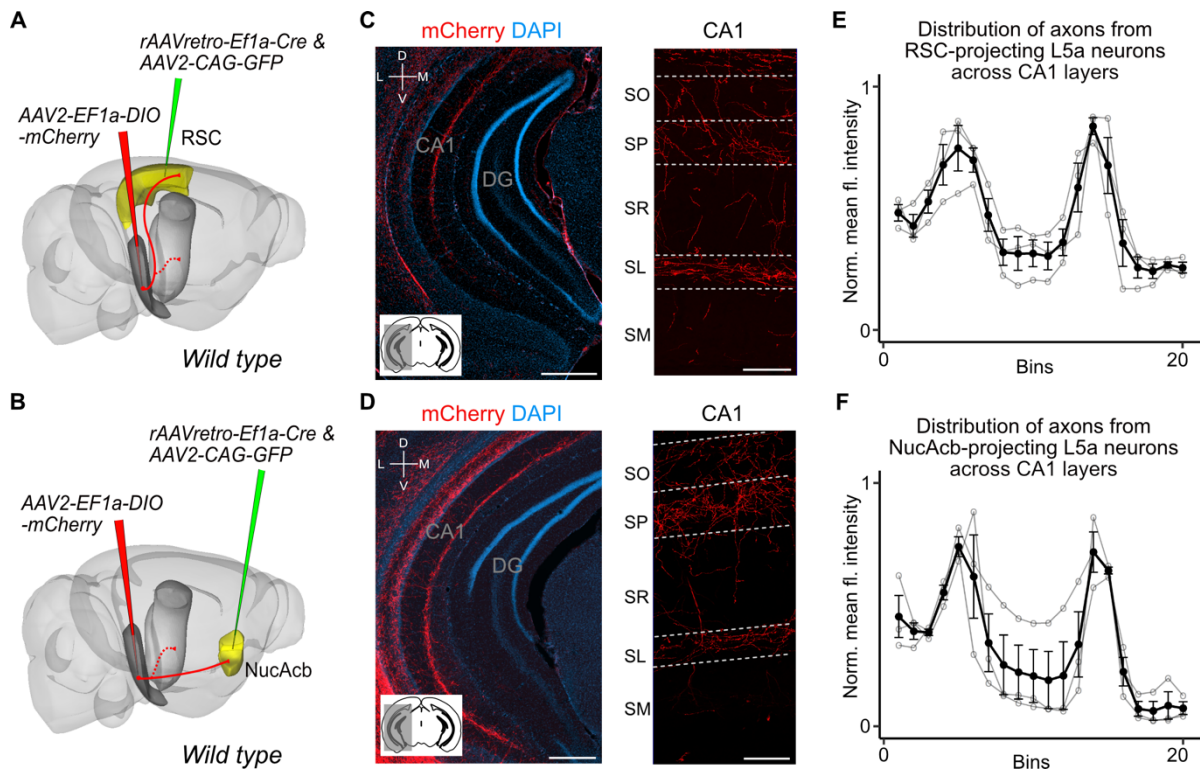
155   telencephalic targets.

Figure 3. Retrosplenial cortex and nucleus accumbens outputs of the MEC are copied to CA1

A, B, Experimental strategy. In wild-type mice, a retrogradely-transported virus expressing Cre was injected in either the retrosplenial cortex (RSC; A) or nucleus accumbens (NucAcb; B), while a Cre-dependent reporter virus was injected in the deep MEC.

C, D, Hippocampal axon collaterals of RSC-projecting (C) or NucAcb-projecting MEC neurons (D; Scale bar: 250 µm). Insets: high-magnification images from CA1 showing distribution of axons across CA1 layers (Scale bar: 100 µm). Bottom-left schematic indicates the antero-posterior position of the slice. Corresponding injection site images are shown in Figure 3- figure supplement 1A and B.

E, F, Quantification of mean fluorescence intensity across the layers of CA1 when only RSC-projecting (E) or NucAcb-projecting (F) MEC neurons were labelled (n = 3 mice for each group). Axon topography is similar to when L5a neurons are marked globally in the *Rbp4-Cre* mice (Figure 2C).

156   Entorhinal cortex outputs have diverse targets, including the entire cortical mantle as well as

157   parts of basal ganglia and amygdala (Swanson and Köhler, 1986, Sürmeli et al., 2015). To

158   test whether axon collateralisation to the hippocampus is a general feature of all

159   telencephalon-targeting neurons, we used Multiplex Analysis of Projections by Sequencing

160   (MAPseq; Kebschull et al., 2016). We injected the MAPseq barcode RNA virus library into

161   the full dorso-ventral extent of the deep MEC (Figure 4- figure supplement 1A) and

162   quantified barcode RNA expression in tissue collected from dorsal and ventral MEC, dorsal

163   and ventral hippocampus and three major divisions of the brain (isocortex, cerebral nuclei

164   (CNU), olfactory areas and cortical subplate (Olf/Ctxsp), see methods for detailed

165   description, Figure 4A). The majority of barcodes that were detected in any one of the three

166   target divisions (isocortex, CNU or Olf/Ctxsp) were also detected in the hippocampus,

167   suggesting that collateral axons to the hippocampus are a common feature of telencephalon-

168   projecting neurons (Figure 4B). The results were similar regardless of whether neurons were

169   located in dorsal or ventral MEC (Figure 4- figure supplement 1B), suggesting that

170   collateralisation does not depend on the neuron's position in the dorso-ventral axis of the

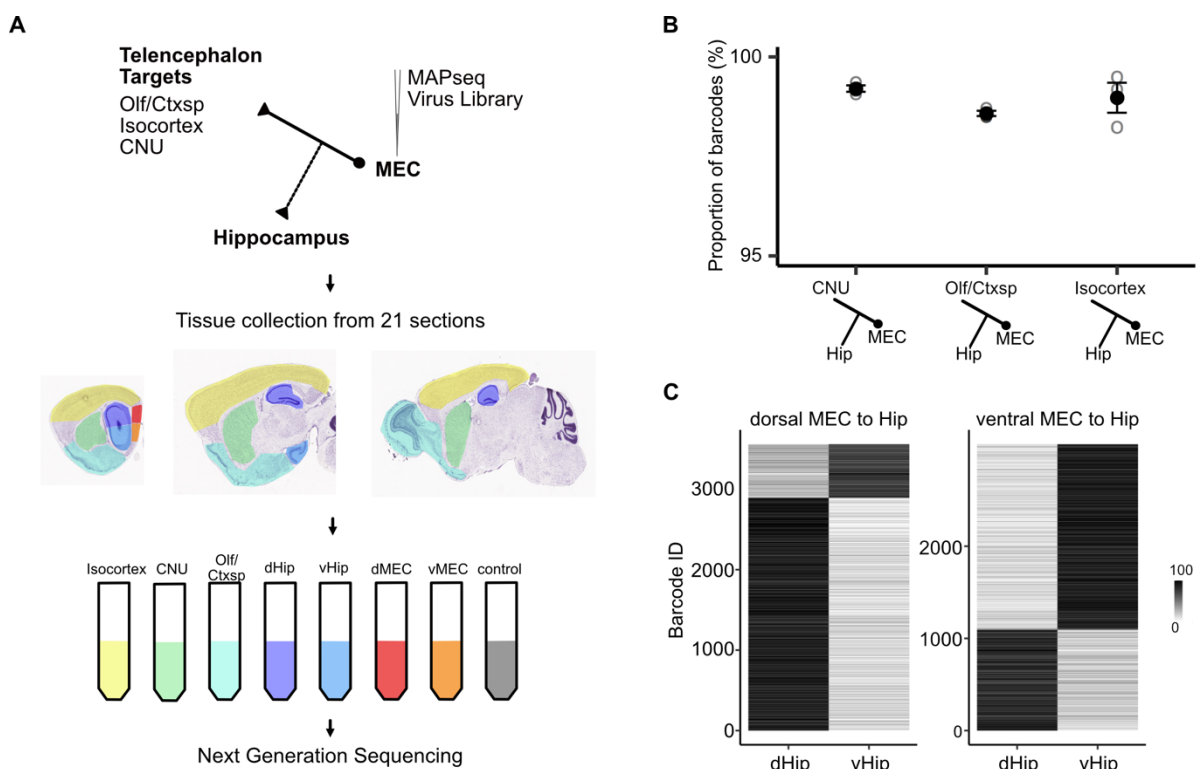171   MEC. Using barcode counts as a measure of projection strength (Kebschull et al., 2016) we

Figure 4. Telencephalic outputs are widely copied onto the hippocampus
A, Experimental strategy. A MAPseq virus library was injected into deep MEC (n = 3). 44 hours later, mice were sacrificed and brains were serially sectioned in the saggital plane at 400 μm thickness. Tissue from 5 major divisions (Isocortex, CNU, Olf/Ctxsp, dHip and vHip), as well as dorsal and ventral MEC were then dissected and collected in tubes. Brainstem tissue was collected as a negative control. Tissue was further processed for RNA extraction and next generation sequencing.
B, Nearly all barcodes detected in CNU, Olf/Ctxsp and Isocortex were also detected in the hippocampus (Isocortex: 98.6% ± 0.06%; CNU: 99.2% ± 0.08%; Olf/Ctxsp: 99.0% ± 0.4%; n = 3 mice, 5358 barcodes).
C, Dorso-ventral topography of projections revealed by relative barcode counts. For each barcode, counts were normalised to show the relative projection strength of each neuron to dorsal and ventral hippocampus (n = 3 mice).

172   further found that dorsal MEC neurons preferentially project to dorsal aspects of the

173   hippocampus and ventral MEC neurons to the ventral aspects, indicating that the back-

174   projections to the hippocampus are topographically organised (Figure 4C). Together these

175   results reveal general organising principles by which all projections from MEC to the

176   telencephalon are copied back to the hippocampus.

177   Which cell types within the hippocampus receive signals from L5a of MEC? While the

178   compartmentalised arrangement of axons from L5a of MEC suggests selective targeting of

179   CA1 layers, axonal topography does not necessarily reflect functional connectivity.

180   Therefore, we targeted viral vectors expressing a channelrhodopsin2-mCherry conjugate

181   to L5a neurons in MEC and tested for connectivity using whole-cell ex-vivo patch clamp

182   recordings from CA1 neurons.

183   We focused initially on responses of pyramidal cells. Brief light pulses evoked depolarising

184   sub-threshold postsynaptic potentials (PSPs) in 64% of SP pyramidal neurons recorded at

185   their resting membrane potential (n = 64 cells, 27 mice, Figure 5A,B,C and Figure 5- figure

186   supplement 1E). The response probability of neurons in distal CA1 was not significantly

187   different than neurons in proximal CA1 (Figure 5D). The majority of PSPs (20 out of 26)

188   maintained their polarity when the membrane potential was adjusted from rest (Vm = -66.7 ±

189   0.6 mV) to -50 mV, indicating that they were glutamatergic. In these neurons EPSPs were

190   maintained when GABA$_A$ receptors were blocked with Gabazine, but were abolished by the

191   AMPA receptor antagonist NBQX, confirming that they are glutamatergic (Figure 5E). The

192   responses had short latencies (3.04 ± 0.26 ms, n = 20 cells, 15 mice) that were relatively

193   invariant from trial to trial (Figure 5F) and were independent of the response's position within

194   a train of stimuli, indicating that they are monosynaptic (Figure 5- figure supplement 1D).

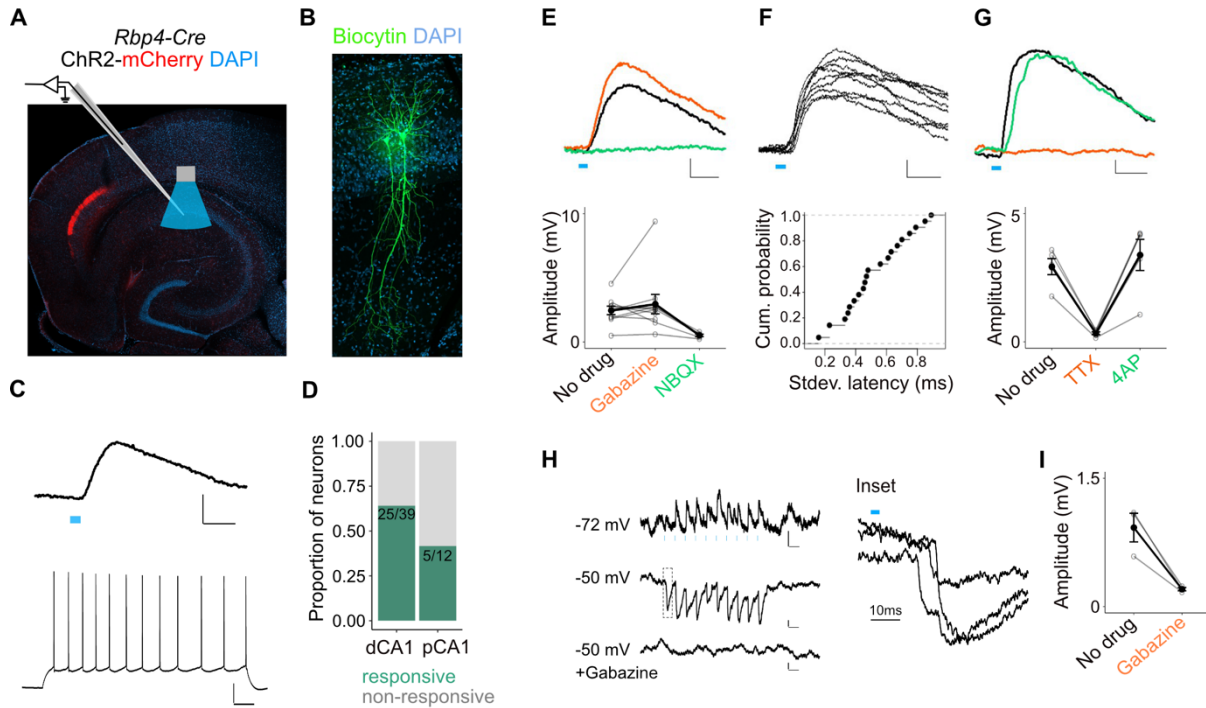195   Consistent with this, responses were sensitive to bath application of tetrodotoxin (TTX) but

Figure 5. L5a neurons of the MEC provide direct excitatory and indirect inhibitory inputs to pyramidal cells in CA1

A, Experimental design showing viral expression, placement of patch-clamp electrode and light delivery over CA1.

B, Examples of biocytin filled pyramidal neurons recorded in CA1.

C, An example electrical recording of a pyramidal neuron at rest (-67 mV) showing depolarizing responses upon 3 ms light stimulation (top) (blue line, Scale bar: 1 mV, 10 ms). Train of action potentials upon 200pA step-current injection (bottom). (Scale bar: 20 mV, 100 ms)

D, Proportion of responsive pyramidal neurons located in the distal and proximal halves of CA1. The difference in proportions was not significant (X-squared = 1.0932, df = 1, p-value = 0.2958, Chi-squared test, n = 12 cells in proximal and n = 39 cells in distal CA1).

E, Effects of bath application of Gabazine (orange, n = 10 cells, 9 mice) and NBQX (green, n = 5 cells) on PSPs recorded from a pyramidal neuron (Scale bar: 0.5 mV, 10 ms) and a summary plot of PSP amplitude measurements for all tested pyramidal neurons. Note that some neurons were only treated with Gabazine which did not cause a significant change in amplitudes (p = 0.97, 2-tailed Student's t-test, n = 10 cells, 9 mice).

F, An example of ten consecutive PSP responses recorded from a single pyramidal neuron illustrates the short and invariant latency of PSPs (Scale bar: 0.5 mV, 10 ms) and a cumulative probability plot of standard deviation of latencies for neurons with PSP responses that were > 1 mV in amplitude (n = 20 cells).

G, Effects of bath application of TTX (orange) and 4-AP (green) on PSPs recorded from a pyramidal neuron (Scale bar: 0.5 mV, 10 ms) and a summary plot of changes in PSP amplitudes for all tested pyramidal neurons. TTX application abolished responses (n = 5 cells, 5 mice, p = 0.01, 2-tailed Student's t-test).

H. An example inhibitory PSP response recorded from a pyramidal neuron upon 10 Hz light stimulation (blue bars). Response polarity reversed when the neuron's membrane potential was adjusted to -50 mV and was abolished after application of Gabazine (Scale bars: 0.2 mV, 100 ms). Inset shows the long latency (> 10 ms) of PSP onset indicating polysynaptic connectivity.

I. Effects of bath application of Gabazine on the response amplitude of long latency PSPs (n = 3 cells).

196   recoverable after application of 4-Aminopyridine (4-AP; Figure 5G; Petreanu et al., 2007).

197   Together, these data demonstrate that projections from L5a of the MEC provide

198   glutamatergic excitatory inputs directly to pyramidal neurons in proximal and distal CA1.

199

200   A smaller population of pyramidal neurons showed PSPs with characteristics of indirect

201   inhibitory connections (6 out of 26). These responses either reversed polarity when the cell

202   was held above the chloride reversal potential (Figure 5H) or had an early depolarising and a

203   late hyperpolarising component (Figure 5- figure supplement 1B). Application of Gabazine

204   either completely blocked the PSPs (Figure 5I) or revealed a larger excitatory component

205   that was sensitive to application of NBQX (Figure 5- figure supplement 1B). Thus, inputs

206   from L5a of the MEC also recruit local interneurons that provide inhibitory input to SP

207   pyramidal neurons.

208

209   To identify which interneurons in CA1 were targets of L5a projections, we tested responses

210   of interneurons in all layers. In SP we distinguished interneurons from principal cells either

211   by classifying them based on biophysical properties (fast-spiking: SP_{FS} and non-fast spiking:

212   SP_{NFS}; Figure 5- Figure supplement 1a and see methods), or by recording from

213   fluorescently-labelled GABAergic or parvalbumin-expressing (PV+) inhibitory neurons in

214   double transgenic mice (Figure 6A,B and Figure 5- figure supplement 1C). Stimulation of

215   L5a axons elicited both sub-threshold and supra-threshold responses primarily in SP, SR

216   and SL interneurons (Figure 6C,D and Figure 5- figure supplement 1E). Depolarising PSPs

217   were observed in 64% of the SP_{FS} including PV+ interneurons, 46% of the SP_{NFS}, 64% of SR

218   and lower proportions of recorded neurons in SL (31%), SM (23%) and SO (16%). Except for

219   interneurons in SO, PSPs in all layers showed characteristics of monosynaptic connectivity

220   (Figure 6G,H,I,J and Figure 5- figure supplement 1G,H) and AMPA receptor-mediated
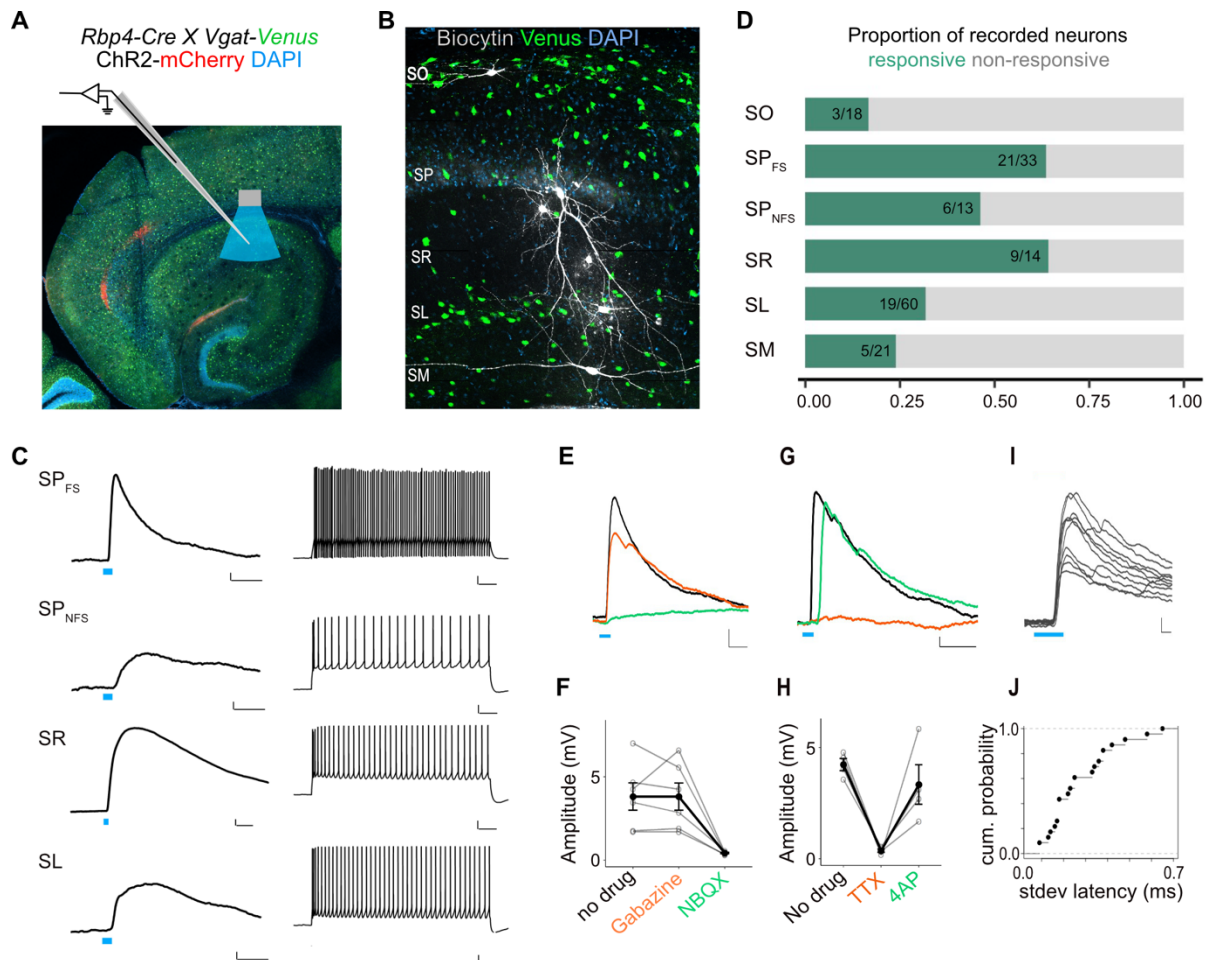
221

222

Figure 6. L5a neurons of the MEC provide direct excitatory inputs to interneurons in CA1.

A, Experimental design showing viral expression, patch pipette and light stimulation. Interneurons are marked by the expression of venus fluorescent protein driven by the vesicular GABA transporter (*Vgat*) gene's promoter.

B, Biocytin filled neurons in the *Rbp4-Cre X Vgat-Venus* double transgenic mouse line. Fluorescent labelling facilitated patch-clamp recordings made from GABAergic interneurons and distinguishing SR, SL and SM layers.

C, Representative examples of depolarising responses recorded at resting membrane potential following 3 ms blue light stimulation (blue line) of L5a axons in CA1 (left) (Scale bar: 1 mV, 10 ms). Neurons in SO and SM were typically not responsive (< 30%). Responses from SR neurons were on average larger than the responses from neurons in other layers (Scale bar: 1 mV, 10 ms). Neurons' spiking response to injecting 200 pA current (right) (Scale bar: 10 mV, 100 ms).

D, Proportion of responsive interneurons in all layers of CA1 recorded at resting membrane potential. Green highlighted segment corresponds to the proportion of cells with depolarising membrane potentials; grey highlighted segment corresponds to neurons with no change in their membrane potential.
SO: n = 18 cells, 10 mice;
SP_{FSint} : n = 33 cells, 8 *Rbp4-Cre X Pvalb-Flp mice*, 5 *Rbp4-Cre X Vgat-Venus mice*, 8 *Rbp4-Cre* mice;
SP_{NSFint}: n = 13 cells, 11 *Rbp4-Cre* mice, 1 *Rbp4-Cre X Vgat-Venus* mouse;
SR: n = 14 cells, 6 mice; SL: n = 60 cells, 15 mice; SM: n = 21 cells, 10 mice

E,F, Effects of bath application of Gabazine (orange) and NBQX (green) on PSPs recorded from a fast-spiking pyramidal layer interneuron (left) (Scale bar: 1 mV, 5 ms)**.** Summary quantification of PSP amplitudes for multiple cells (right). The PSP amplitudes were largely unaffected by application of Gabazine (SP_{int} : n = 6 cells, p = 0.99 2-tailed Student's t test) but were largely blocked by NBQX (SP_{int} : n = 5 cells, p = 0.03, 2-tailed Student's t test) indicating AMPA receptor mediated glutamatergic synaptic transmission.

G,H. Effects of bath application of TTX (orange) and 4-AP (green) on the response amplitude PSPs recorded from pyramidal layer interneurons. Example traces from a fast-spiking pyramidal layer interneuron (Scale bar: 1 mV, 5 ms). Summary plots of response amplitude measurements from multiple recordings (SP_{int}: n = 4 cells).

I, J, An example of ten consecutive PSP responses recorded from a single fast-spiking interneuron in SP illustrates the short and invariant latency of PSPs. Cumulative probability plots of standard deviation of latencies for neurons with PSP responses that were > 1 mV in amplitude (mean latency SP: 2.08 ± 0.08 ms, n = 21 cells).

223   glutamatergic synaptic transmission (Figure 6E,F and Figure 5- figure supplement 1F).

224   Therefore, projections from L5a of MEC recruit CA1 interneurons through monosynaptic

225   inputs driven by excitatory glutamatergic synapses.

226   **Discussion**

227   Together our results suggest a substantial revision to the idea that the entorhinal deep layers

228   unidirectionally convey hippocampal output messages to the neocortex. Using two lines of

229   evidence, combinatorial viral labelling and MAPseq, we show that L5a axons bifurcate to

230   target both the telencephalon and the hippocampus. Our results imply that nearly all

231   telencephalic output is copied onto the hippocampus regardless of its destination in the

232   telencephalon. There is a topographical register between the dorso-ventral origin of the

233   entorhinal cells and their target zone within the hippocampus. This is similar to the dorso-

234   ventral topography of perforant-path projections of the superficial EC targeting the dentate

235   gyrus, supporting the view that dorso-ventral compartments of the hippocampus operate

236   independently (Ruth et al., 1982; Dolorfo and Amaral 1998). Interestingly in the transverse

237   axis, the density of projections has a gradient descending towards proximal CA1 (towards

238   CA2). This is in contrast to previous reports where labelling of MEC projections using

239   traditional tracers revealed dense projections in proximal but not in distal CA1 (Tamamaki

240   and Nojyo, 1995; Naber et al., 2001). Instead, distal CA1 is thought to be primarily targeted

241   by the lateral EC. The distinct organization of projections originating in L5a of the MEC that

242   we reveal here suggests that they serve functions distinct from the projections targeting CA1

243   from superficial layers instead of merely supplementing them (Witter et al., 2017). This also

244   opens a possibility for the lateral and medial entorhinal cortex input streams to converge in

245   CA1.

246

247   Although cells in deep entorhinal layers have been previously observed when retrograde

248   dyes were placed in the CA1-subiculum border (Köhler, 1985; Witter and Amaral, 1991) the

249   tools we introduced in this study made it possible to investigate the layer origin of these

250   projections and their targets within CA1 with cell type specific anterograde labeling. Our

251   observation that L5b does not participate in this pathway reinforces the distinct input-output

252   organisation of the deep MEC. While L5b is a point of integration for local and neocortical

253   input with hippocampal output and distributes its signals locally within MEC, L5a appears to

254   be suited to coordinate the wider hippocampal-neocortical loop by providing a copy of

255   entorhinal output back to CA1.

256

257   Finally, our findings raise new questions about the functional roles of outputs from the

258   entorhinal cortex, and about the nature of interactions between the entorhinal cortex and the

259   hippocampus. Telencephalic projections of L5a cells have been shown to be necessary for

260   long-term memory formation and retrieval (Kitamura et al., 2017), likely by distributing

261   compressed hippocampal outputs to the neocortex (McClelland et al., 1995). Returning a

262   copy of these outputs back to CA1 might create a self-reinforcing or a self-correcting loop.

263   They might also provide a gating signal to modulate the impact in CA1 of inputs from CA3

264   (Dudman et al., 2007) and/or neocortical return inputs via L3 of EC. It is also conceivable

265   that they influence mechanisms of learning and memory by affecting rhythmic network

266   activity through the inputs on the pyramidal cells and interneuron populations that we

267   described here (Colgin 2016; Ognjanovski et al. 2017; Xia et al. 2017).

268

269

270

271

272

273

274

275

276

277 **Methods**

278 Mice

279 All animal experiments were approved by the University of Edinburgh animal welfare

280 committee and were performed under a UK Home Office project license. The *Rbp4-Cre*

281 mouse line was generated by GenSat and obtained from MMRRC (*Tg(Rbp4-*

282 *cre)KL100Gsat/Mmucd*). The *Vgat-Venus* mouse line was generated by Dr. Atsushi

283 Miyawaki at RIKEN, Wako, Japan(Wang et al., 2009). The *Pvalb-Flp* mouse line was

284 obtained from Jackson Laboratories *(B6.Cg-Pvalb-tm4.1(FlPo)Hze/J; Jax 022730)*. Wild-type

285 mice were obtained from Charles River Laboratories C57Bl6J stock. Double transgenics

286 were generated by crossing the *Rbp4-Cre* line to the *Vgat-Venus* or the *Pvalb-Flp* lines.

287 *Rbp4-Cre* and *Pvalb-Flp* lines were maintained as heterozygous and all mice were on

288 C57Bl6 background.

289 Viral constructs and injection strategy

290 8 to 14 week-old male and female mice were used in all experiments. For targeting deep

291 MEC a craniotomy was made 3.4 to 3.65 mm lateral to the bregma (X) between the

292 transverse sinus and lambdoid suture (Y = 4.5 to 5 mm caudal to bregma). The injection

293 pipette was at a 9 degree angle towards the caudal end of the brain. 100 nl of virus was

294 slowly released at four Z-depths 3.0, 2.8, 2.6 and 2.4 mm from the surface of the brain. 3

295 mins after delivering the virus the injection needle was retracted to the next injection depth

296 until the most dorsal location where 10 mins past before the needle was fully retracted. For

297 anterograde tracing of L5a axons and terminals *AAV-EF1a-DIO-mCherry* (serotypes 2 and

298 5, titer 5.3 x 10^{12}, lot #AV4375H, K., Deisseroth, UNC Vector Core), *AAV-CAG-FLEX-GFP*

299 (titer 3.7 x 10^{12}, lot #AV4530B, E. Boyden, UNC Vector Core) and AAV-hSyn-FLEx-mGFP-

300 2A-Synaptophysin-mRuby (Addgene:71760) were used.

301 For injections in CA1 a craniotomy was made 3.5 mm lateral and 3.30 mm caudal to the

302 bregma in C57BL6J mice. 100nl virus was delivered at 3.0, 2.8, 2.6, 2.4 and 2.2 mm from

303 the surface. For retrograde labelling of hippocampus-projecting EC neurons, 100nl of a

304 *rAAV2retro-CAG-GFP* (titre 3.5 x 10^{12}, lot #AV7493D, E. Boyden, UNC Vector Core) or

305 *rAAV2retro-hSyn-mCherry* (E. Boyden, UNC Vector Core) was injected at each depth.

306 To assess whether telencephalic projection neurons in L5a of MEC co-express Etv1 (Figure

307 1- figure supplement 1D), fluorophore coupled choleratoxin beta subunit (CTB-Alexa 488

308 and CTB-Alexa 555) was injected at various sites in wild-type mice as previously described

309 (Sürmeli et al., 2015) and coexpression of Etv1 and Alexa dyes were examined in confocal

310 images.

311 To achieve Cre expression in target specific subpopulation of L5a neurons in the MEC

312 (Figure 3) a *rAAVretro-EF1a-Cre-WPRE* (viral construct was a gift from Karl Deisseroth, titre

313 2.4 x 10^{12}) was made using an AAV-retro helper plasmid (Addgene plasmid ID 81070) as

314 described previously(McClure et al., 2011). A cocktail of *rAAVretro-EF1a-Cre-WPRE* and

315 *AAV-CAG-GFP* (titer 4.3 x 10^{12}, lot #AV6951B, Boyden, UNC Vector Core) viruses were

316 injected either in NucAcb (X: +1.0 mm; Y: +1.2 mm; Z: -3.8, -4.0 mm) or RSC (X: +0.4 mm;

317 Y: -2.8, -3.2 mm; Z: -0.9 mm) in wild-type mice. A Cre inducible reporter virus was also

318 injected in the MEC as described above. GFP expression driven by the *CAG* promoter at the

319 target site was used for verification of injection location.

320 To achieve expression of channelrhodopsin-2 in L5a axons, we injected *AAV2-EF1a-DIO-*

321 *hChR2(H134R)-mCherry-WPRE-pA* (titer 5.1 x 10^{12}, lot #AV4319J, Deisseroth) in the MEC

322 of the *Rbp4-Cre* or the *Rbp4-Cre X Vgat-Venus* or the *Rbp4-Cre X Pvalb-FLP* double

323 transgenic mice. Additionally, in order to fluorescently label parvalbumin expressing

324 interneurons in CA1 a Flp recombinase-dependent AAV vector was constructed in house

325 and injected in the hippocampus (X: +3.0 mm; Y: -3.5 mm; Z: -2.0, -3.0 mm, 200 nl virus was

326 injected at each Z-depth). To produce the virus, the viral construct pAM-FLEX-GFP(Murray

327   et al., 2011) (a gift from Peer Wulff) was used as the viral backbone. The eGFP, loxP and

328   lox2272 sites were removed and replaced with a synthesised cassette (GenScript)

329   containing a multiple cloning site flanked by two sets of heterotypic (FRT and F3),

330   antiparallel FRT sites to produce pAM FLPX. For pAM FLPX eGFP and pAM FLPX mCherry,

331   the fluorescent proteins were amplified from pAM FLEX eGFP and pmCherry-C1 (Clontech)

332   respectively, with EcoRI and SacI overhangs and cloned into pAM FLPX. All AAV preps

333   were generated in house as previously described(McClure et al., 2011) and were titered by

334   qPCR following expression in HEK cells (> 10^{12} genome copies (GC)/ml).

Tissue processing and immunohistochemistry

336   3 to 4 weeks after the virus injection surgery, mice were transcardially perfused with 4%

337   paraformaldehyde as previously described(Sürmeli et al., 2015). Brains were sectioned at 60

338   μm using a cryostat (Leica CM3050 S) either coronally or horizontally and sections were

339   stored in PBS at 4◦C. All subsequent incubation and washing steps were carried out at 4◦C.

340   Prior to antibody staining, sections were blocked with either 5% normal goat serum (NGS;

341   Abcam: ab13970) or 2% bovine serum albumin (BSA; Sigma: A9418) in 0.3% PBST (PBS

342   with 0.3% Triton-X100) for 2hrs. Sections were then transferred to primary antibody solutions

343   made with either 5% NGS or 2% BSA in 0.3% PBST and incubated overnight. After 3

344   washes, each 20 min, in 0.3% PBST, sections were transferred to secondary antibody

345   solutions made with 0.3% PBST and, if required, NeuroTrace 640/660 (1:800; Life

346   Technologies: N21483) and incubated overnight. After 3 washes, sections were incubated in

347   DAPI (1:2,000; Sigma Aldrich: D9542) solution made in PBS for 20 min at room temperature,

348   where required, and then mounted on microscope slides using Mowiol® 4-88 (Aldrich:

349   81381). Slides were covered with glass coverslips and left to dry overnight at 4◦C in the dark.

350   The following primary antibodies were used: rat anti-mCherry (1:2,000; ThermoFisher:

351   M11217), chicken anti-GFP (1:10,000; Abcam: ab13970), rabbit anti-Etv1(Arber et al., 2000)

352   (1:1,000), chicken anti-NeuN (1:1,000; Sigma Aldrich: ABN91). The following secondary

353   antibodies from Thermo Fisher Scientific were used at a concentration of 1:800: goat anti-

354   rabbit A488 (A11034), goat anti-chicken A488 (A11039), goat anti-rat A555 (A21434) and

355   goat anti-rabbit (A21244).

356   Cell counting

357   Every 4th brain section was imaged as a Z-stack (1 μm step size) using either the Zeiss

358   LSM 800 (Zen, v2.6.76) or Leica SP8 confocal microscope (Leica Application Suite X,

359   v3.5.6.21594) at 20x magnification. Regions of interest were drawn around L5a and cell

360   counting was carried out either manually using Fiji software or using cell-counting tools in

361   Vision4D (Arivis, v3.2.0).

362

363   The boundaries for L5a were determined using either a DAPI or Neurotrace counterstain.

364   The border between medial and lateral divisions of EC was determined in each section using

365   layer 2 as a guide – in lateral EC, layer 2 is separated into two distinct layers, while this

366   separation is not seen in medial EC(Cappaert et al., 2015).

367   Quantification of the distribution of fluorescent signal

368   *Quantification of fluorescence across the radial axis of the CA1*

369   The distribution of axons of L5a neurons in the radial axis of the hippocampal CA1 was

370   quantified in slide-scanner images (Figure 2) or confocal images (Figure 3) using Fiji

371   software. Coronal brain sections between 3.28 to 3.58 mm posterior to Bregma, which

372   contain distal CA1, were selected for analysis. 2 sections from each brain in which the

373   fluorescent labeling was representative of all the sections were used. DAPI was used as a

374   counterstain. In each section, a 400 μm-wide rectangular ROI was drawn across the radial

375   axes, covering all layers of a randomly selected region in intermediate CA1 (Figure 2B). This

376   ROI was then divided into 20 equal bins and the mean fluorescence intensity was calculated

377   for each bin. The mean intensity values were then normalised in each brain by scaling the

378   values such that the highest value is 1.

379   *Quantification of fluorescence in the transverse axis of the CA1*

380   A Zeiss Axioscan slidescanner was used to image every second brain section at 10x

381   magnification. The projection strengths of MEC L5a neurons to proximal and distal halves of

382   CA1 were quantified in horizontal sections located at depths between 2.56 mm to 4.12 mm

383   from the surface of the brain, with injection sites located across medial, mid and lateral MEC

384   (15-18 brain sections per mouse, n = 5 mice). GFP and mCherry fluorescence signals were

385   amplified with immunostaining as described previously. The borders of CA1 were drawn on

386   brain section images using a customisable digital microscopy analysis platform (Visiopharm),

387   and the proximo-distal border was defined as the border equidistant from the proximal and

388   distal ends of CA1. The mean fluorescence density, defined as the total number of pixels

389   above a set threshold in an area divided by the total number of pixels in the area, was

390   measured in proximal and distal CA1. The threshold was determined manually by ensuring

391   that only pixels representing axons were detected as signal. A median unsharp background

392   correction was used to remove background noise from axons outside of the focus plane of

393   the image. The mean fluorescence density values were then normalised within each brain by

394   scaling the values such that the total fluorescence density value (proximal + distal) in each

395   brain is equal to 1.

396   The spread of viral expression in MEC was assessed from the fluorescent signal in all

397   sections for each brain. Brains in which labelled neurons were found outside L5 were

398   excluded; this was a result of occasional and sparse labelling in L2 or L3 or the

399   parasubiculum in the *Rbp4-Cre* line.

400   MAPseq

401 5 C57Bl6J adult male and female mice were injected in the deep MEC with the MAPseq

402 Sindbis viral barcode library (3 x 10^{10} GC/ml) provided by the MAPseq facility (Cold Spring

403 Harbor Laboratories). To cover the whole mediolateral and dorsoventral extent of the MEC

404 virus was injected in two locations: 3.4 mm and 3.6 mm lateral to bregma. 100 nl virus was

405 delivered to 3.0, 2.8, 2.6, 2.4 mm below the surface of the brain. After 44 hrs, mice were

406 sacrificed, brains were extracted and immediately immersed in oxygenated cold ACSF

407 prepared in ultrapure water. All surgical tools and surfaces were treated with RNaseZAP

408 (Invitrogen) prior to the start of the experiment and in-between samples. 400 μm fresh

409 sagittal brain sections were cut using a vibratome(Pastoll et al., 2012). Immediately after

410 this, GFP expression in the deep EC was verified under a fluorescent microscope and tissue

411 was dissected in cold oxygenated ACSF using microdissection blades on sylgard covered

412 petri dishes which were kept on ice. Each slice was dissected on a previously unused

413 surface of the plate with fresh ACSF and a dedicated microblade was used for the dissection

414 of each brain division to prevent contamination. Tissue pieces were collected into bead

415 containing (Qiagen 69989) collection tubes (Qiagen 19560) on dry ice. After tissue

416 collection, 400 μl Trizol (Thermo Fisher Scientific #15596026) was added to each collection

417 tube. The procedure was repeated for all 5 brains. 3 brains with the largest coverage of MEC

418 deep layers were selected to proceed to the next steps. Tissue was stored at -80 degrees

419 before it was shipped on dry ice to CSHL MAPseq core facility for further processing. RNA

420 extraction, production of double stranded cDNA, library preparation and Illumina sequencing

421 and preprocessing of sequencing data was performed by the MAPseq core facility as

422 described in(Kebschull et al., 2016).

423 For the tissue dissections, identification of brain areas was done by using Allen Brain

424 Reference Atlas (https://mouse.brain-map.org/). The isocortex division included the

425 somatosensory, motor, visual, posterior parietal, anterior cingulate and retrosplenial areas

426 combined. The cerebral nuclei (CNU) division was restricted to striatum. The

427 olfactory/cortical subplate division (Olf/Ctxsp) was a combination of olfactory areas and

428   cortical subplate including amygdalar nuclei. The remaining two divisions were dorsal (dHip)

429   and ventral hippocampus (vHip) including subiculum. Some brain areas were excluded from

430   the study because of the difficulty in dissecting or identifying brain areas in the sagittal plane.

431   All sections > 3.7 mm lateral to bregma are not annotated in Allen Brain Reference Atlas and

432   were excluded. Therefore, neocortical areas in the most lateral sections such as perirhinal

433   cortex, ectorhinal cortex, temporal association areas were not included in the study. The

434   claustrum and adjacent neocortical areas (visceral, agranular insular, gustatory) were

435   excluded as it was not possible to separate these areas precisely to prevent contamination

436   between the assigned divisions. Since borders between the brain divisions CNU and

437   OLF/Ctxsp were not always clear, dissections avoided these areas hence the brain areas in

438   these divisions are partially included. White matter between the hippocampus and the

439   neocortex carrying axon tracts were also excluded. Brainstem and cervical spinal cord tissue

440   were used as control. When L5a neurons in the MEC were labelled using strategies

441   explained in Figure 2, no axonal projections to these areas were observed (unpublished

442   experiments). Consistent with this, a low number of barcodes were identified in the negative

443   control samples (on average 1.0% of barcodes had counts in control areas, n = 3).

444   A limitation of the barcode-based single-cell tracing method comes from the possibility of

445   multiple neurons being represented by the same barcode. This is prevented by adjusting the

446   barcode diversity and the size of the target population as explained in detail in(Kebschull et

447   al., 2016). In order to assess the expected fraction of uniquely labelled neurons in our study

448   we counted the total number of neurons in L5a of the MEC. A total of 2314 ± 131, (n = 2

449   mice) NeuN-labelled neurons were counted. Using the formula $F = (1-(1/N))^{k-1}$ where N is

450   the barcode diversity (2×10^6)(Kebschull et al., 2016) and k is the number of infected

451   neurons the predicted ratio of uniquely labelled neurons is 99.9%. Multiple representation of

452   neurons due to a neuron being infected by several different barcode RNA-expressing viral

453   particles was not corrected for since the projection patterns are not affected by

454   overrepresentation of neurons(Kebschull et al., 2016).

455   *MAPseq data analysis*

456   Barcode counts were first normalised in each area by the relative number of spike-in RNAs

457   for each sample. Orphan barcodes, barcodes which did not have counts in the injection site,

458   (dMEC or vMEC) were removed. We then calculated the 95th percentile of the barcode

459   counts in our negative controls and based on this set all barcode counts of 1 to 0. A small

460   number of barcodes had a higher count in any target area compared to the injection site

461   which might be a result of incomplete dissection of the injection site or viral expression in

462   areas that the virus spilled into as we retracted the pipette. These barcodes were removed.

463   Since our goal was to find whether neurons projecting to the telencephalon also project to

464   the hippocampus we removed the barcodes that had no counts in any of the telencephalic

465   target areas. For the same reason, barcodes that were detected only in the dHip or vHip

466   hippocampus were also removed. Finally, we excluded all barcodes with counts of less than

467   400 in the injection site to minimise the possibility of incomplete transport of RNA barcodes

468   to axons in target areas due to weak expression at the cell bodies or low counts due to PCR

469   or polymerase errors. Barcodes with low counts in all target areas (< 10) were also excluded

470   to account for potential false positives.

471

472   To quantify the proportion of barcodes that were present in both a target division (Figure 3H;

473   Isocortex, CNU or Olf/Ctxsp) and the hippocampus, the following formula was used: (total

474   number of barcodes with counts detected in both hippocampus and target division / total

475   number of barcodes with counts detected in target division). To compare the difference

476   between barcodes with the injection site in dMEC vs vMEC, the barcodes were divided into

477   two groups – "dorsal MEC", where counts in dMEC were higher than in vMEC, and vice

478   versa for "ventral MEC". A paired two-tailed Wilcoxon signed rank test was used to check if

479   there was a significant difference between the proportion of collateralising neurons in dMEC

480   and vMEC.

481

482   To visualise the distribution of barcode counts in dHip and vHip from "dorsal MEC" or

483   "ventral MEC" groups, we generated heat maps showing normalised projection strengths

484   between dHip and vHip for all barcodes. The normalised projection strengths were

485   calculated by the formula: projection strength$_{dHip}$ = (counts$_{dHip}$) / (counts$_{dHip+vHip}$) * 100, and

486   likewise for vHip. Barcodes were sorted by maximum projection site.

487

488   # Ex-vivo electrophysiology

489   *Slice preparation*

490   Slice preparation and subsequent data acquisition was done as previously

491   described(Sürmeli et al., 2015). 3 to 4 weeks after the injection of the viral vectors ex-vivo

492   brain slices were prepared. Following decapitation, brains were immersed for 2 mins in 4°C

493   artificial cerebrospinal fluid (ACSF) of the following composition (mM): 86 NaCl, 1.2

494   NaH_2PO_4, 2.5 KCl, 25 $NaHCO_3$, 25 Glucose, 75 Sucrose, 0.5 $CaCl_2$, 7 $MgCl_2$, bubbled with

495   95% O_2 / 5% CO_2. They were then sectioned horizontally (400 μm) using a vibratome (Leica

496   VT1200) ACSF. Tissue was collected and maintained in extracellular solution of the

497   following composition (mM): 124 NaCl, 1.2 NaH_2PO_4, 2.5 KCl, 25 $NaHCO_3$, 20 Glucose, 2

498    $CaCl_2$ and 1 $MgCl_2$, continuously supplied with 95% O_2 / 5% CO_2. Slices were allowed to rest

499   for 15 mins at 35°C followed by a minimum of 30 mins recovery time at room temperature

500   before the start of the experiment.

501   *Electrophysiological recordings*

502   Whole-cell patch-clamp recordings were made in pyramidal neurons and interneurons in all

503   layers of hippocampal CA1. Typically, 2 to 3 slices from the intermediate hippocampus were

504   used where morphologies of the pyramidal cells and interneurons were confirmed to be

505   intact with post hoc staining and imaging of biocytin filled neurons. Data was collected using

506   AxoGraph (v1.7.6) software.

507   Pipettes with 4 to 6 MΩ resistance were pulled from borosilicate glass (Sutter Instruments)

508   and filled with an intracellular solution of following composition (mM): 130 K Gluconate, 10

509   KCl, 10 HEPES, 2 $MgCl_2$, 0.1 EGTA, 2 Na_2ATP, 0.3 Na_2GTP, 10 NaPhosphocreatine, 5.4

510   Biocytin. The intracellular solution was adjusted to a pH of 7.2 to 7.4 with KOH and

511   osmolarity 290-300 mOsm. All recordings were made in current clamp mode with pipette

512   capacitance neutralisation and bridge balance applied. Subthreshold membrane properties

513   were measured from the changes in membrane potential upon depolarising and

514   hyperpolarising current injections (typically -40 pA to +40 pA, in 20 pA). Rheobase was

515   established from responses to a depolarizing current ramp (50 pA/sec, maximum current

516   400 pA).

517   For optogenetic stimulation of ChR2, an LED of wavelength 470 nm (ThorLabs) was

518   attached to the epifluorescence port of the microscope. Where necessary, the irradiance of

519   the LED (max 9 mW) was controlled by voltage commands. Pharmacological tests were

520   done by bath application of the following reagents with the indicated final concentrations in

521   standard extracellular solution: Gabazine (10 µM, Hello Bio, Cat. No. HB0901), NBQX (10

522   µM, Tocris, Cat. No. 0373), D-AP5 (50 µM, Tocris, Cat. No. 0106), 4-AP (200 µM, Tocris,

523   Cat. No. 0940), TTX (1 µM, Hello Bio). To allow for morphological reconstructions cells were

524   filled with Biocytin (5.4 mM in intracellular solution, Sigma, Cat. No. B4261) during

525   electrophysiological recordings.

526   *Analysis of electrophysiological recordings*

527   Electrophysiological properties were analysed using built-in and custom routines in

528   IGORpro8 (WaveMetrics) and Matlab (MathWorks). All basic properties were established

529   from the I-V protocol described above. Input resistance was determined from the largest

530   depolarising current step injected. Sag ratio was calculated as $V_{steady\ state}/V_{min}$ from the largest

531   hyperpolarising current step. Rheobase and action potential (AP) threshold were determined

532   from the first AP during injection of steadily increasing current in a ramp. From the same

533   protocol, after-hyperpolarisation (AHP) was calculated as the difference between AP

534   threshold and the most negative peak of the hyperpolarisation following the first spike. Half-

535   width was measured as the width of the AP at half its maximum spike amplitude. Firing

536   frequency was measured from a 1 s current injection of 200 pA. Maximum firing frequency

537   was measured between the first two APs, and base frequency between the last two APs in a

538   train.

539   For optogenetic stimulations, responsiveness was confirmed for each cell by a significant

540   difference between the detected peak of change in membrane potential after light stimulation

541   and the average baseline using a 2-tailed, type 1 student's t-test. The PSP amplitude and

542   latency were measured using the Neuromatic toolbox in IGORPro8.

543   Cell types were determined based on biophysical properties extracted from

544   electrophysiology data. Pyramidal cells were identified from a max firing frequency of < 50

545   Hz, AHP < 10 mV, AP half-width ≥ 0.7 ms and sag ≤ 0.9, with descending hierarchical order.

546   Fast spiking interneurons were categorised from a max firing frequency ≥ 100 Hz, AHP ≥ 12

547   mV, AP half-width < 0.5 ms and sag > 0.9. Non-fast spiking interneurons were classified

548   from a max firing frequency 50-100 Hz, AHP ≥ 12 mV, AP half-width 0.5 to 0.9 ms, sag ratio

549   > 0.9. and max firing frequency 50-100 Hz.

550   Neurons with a resting membrane potential less negative than -50 mV or a bridge balance

551   higher than 40 MΩ were excluded from the analysis, as were neurons that did not fit within a

552   class from above criteria.

553   *Immunostaining of electrophysiology slices*

554   For identification of cells following recordings, tissue was fixed in 4% PFA overnight at 4◦C.

555   Slices were washed with PBS three times, 20 min each, and incubated in Streptavidin-Alexa

556   488 (S11223) or Alexa 647 (1:500, S32357, Invitrogen) and DAPI (1:1000, in 0.3% PBST)

557   overnight at 4°C. Slices were washed in 0.3% PBST four times and mounted on glass slides

558   with Mowiol® 4-88. Mcherry fluorescence in the MEC was examined with confocal imaging

559   and those animals where virus injection missed MEC L5 were excluded.

560   For staining of the interneuron marker parvalbumin (PV), slices were prepared as described

561   above, then incubated in primary antibody solution containing mouse anti-PV (1:1000, PV

562   235, Swant) and 5% NGS in 0.3% PBST for 48 hrs at 4°C. Slices were then washed and

563   incubated in secondary antibody solution with Alexa-conjugated Streptavidin and DAPI

564   prepared in 0.3% PBST and mounted on glass slides after overnight incubation.

565   A Zeiss LSM800 microscope was used for image acquisition of the slices. Pinhole was set to

566   1 Airy Unit. Objectives used include x10 (air), x20 (air) and x40 (oil) to image the

567   hippocampal formation, morphology of biocytin filled cells, and immunolabelling of

568   interneurons, respectively.

569   **Image processing and generation**

570   Experimental design sketches were generated using brainrender (Claudi et al., 2021) or

571   Affinity Designer. Where necessary images were cropped and size-adjusted using

572   Photoshop, Pixelmator and ImageJ softwares.

573   Statistics

574   Statistical tests (Student's t-test, Chi-squared test, Wilcoxon signed rank test) were

575   performed using R (www.r-project.org) 3.6.0, 4.0.0 and 4.0.3. Normality was tested for using

576   both the Shapiro-Wilk test and QQ plots. All data is presented in the format of mean ± SEM

577   unless otherwise stated. A p-value < 0.05 was regarded as significant.

578   **Data availability**

579   On publication data and analysis scripts will be made publicly available via University of

580   Edinburgh's Datashare service (http://datashare.is.ed.ac.uk/). This is an online data

581   repository maintained by the University. MAPseq data will be made available at NLM

582   Sequence Read Archive BioProject.

Code availability

584   Analysis script will be made publicly available upon publication via University of Edinburgh's

585   Datashare service

586

595

Contributions

597   S.Y.T. and M.Ö. equally contributed to the study.

598   G.S. conceptualised the study, acquired funding and administered the project. G.S. and

599   S.Y.T. performed MAPseq experiments and analysed the data. M.Ö., G.S. and E.S.

600   performed electrophysiology experiments and data analysis. Anatomy and histology

601   experiments were performed and analysed by S.Y.T., G.S., M.Ö., E.S., and M.R.. C.M.

602   developed reagents. Z.B. developed analysis tools and contributed to early discussions.

603   G.S., S.Y.T., E.S. and M.Ö. prepared the original manuscript.

604

References

606   Arber, S., Ladle, D.R., Lin, J.H., Frank, E., and Jessell, T.M. (2000). ETS gene Er81 controls
607   the formation of functional connections between group Ia sensory afferents and motor
608   neurons. Cell *101*, 485–498.

609   Beed, P., de Filippo, R., Holman, C., Johenning, F.W., Leibold, C., Caputi, A., Monyer, H.,
610   and Schmitz, D. (2020). Layer 3 Pyramidal Cells in the Medial Entorhinal Cortex Orchestrate
611   Up-Down States and Entrain the Deep Layers Differentially. Cell Rep. *33*, 108470.

612   Cappaert, N.L.M., Van Strien, N.M., and Witter, M.P. (2015). Chapter 20 - Hippocampal
613   Formation. In The Rat Nervous System (Fourth Edition), G. Paxinos, ed. (San Diego:
614   Academic Press), pp. 511–573.

615   Claudi, F., Tyson, A.L., Petrucco, L., Margrie, T.W., Portugues, R., and Branco, T. (2021).
616   Visualizing anatomically registered data with brainrender. Elife *10*.
617
618   Colgin, L.L. (2016). Rhythms of the hippocampal network. Nature Reviews Neuroscience *17*,
619   239–249.

620   Czajkowski, R., Sugar, J., Zhang, S.-J., Couey, J.J., Ye, J., and Witter, M.P. (2013).
621   Superficially projecting principal neurons in layer V of medial entorhinal cortex in the rat
622   receive excitatory retrosplenial input. J. Neurosci. *33*, 15779–15792.

623   Dolorfo, C. L., and D. G. Amaral. 1998. Entorhinal Cortex of the Rat: Topographic
624   Organization of the Cells of Origin of the Perforant Path Projection to the Dentate Gyrus. The
625   Journal of Comparative Neurology 398 (1): 25–48.
626
627   Dudman, J.T., Tsay, D., and Siegelbaum, S.A. (2007). A role for synaptic inputs at distal
628   dendrites: instructive signals for hippocampal long-term plasticity. Neuron *56*, 866–879.

629   Frankland, P. W. & Bontempi, B. The organization of recent and remote memories. *Nat. Rev.*
630   *Neurosci.* **6**, 119–130 (2005).
631
632   Gerfen, C.R., Paletzki, R., and Heintz, N. (2013). GENSAT BAC cre-recombinase driver
633   lines to study the functional organization of cerebral cortical and basal ganglia circuits.
634   Neuron *80*, 1368–1383.

635   Kebschull, J.M., da Silva, P.G., Reid, A.P., Peikon, I.D., Albeanu, D.F., and Zador, A.M.
636   (2016). High-Throughput Mapping of Single-Neuron Projections by Sequencing of Barcoded
637   RNA. Neuron *91*, 975–987.

638   Ketz, N., Morkonda, S.G., and O'Reilly, R.C. (2013). Theta coordinated error-driven learning
639   in the hippocampus. PLoS Comput. Biol. *9*, e1003067.

640   Khodagholy, D., Gelinas, J.N., and Buzsáki, G. (2017). Learning-enhanced coupling
641   between ripple oscillations in association cortices and hippocampus. Science *358*, 369–372.

642   Kitamura, T., Pignatelli, M., Suh, J., Kohara, K., Yoshiki, A., Abe, K., and Tonegawa, S.
643   (2014). Island Cells Control Temporal Association Memory. Science *343*, 896–901.

644   Kitamura, T., Ogawa, S.K., Roy, D.S., Okuyama, T., Morrissey, M.D., Smith, L.M., Redondo,
645   R.L., and Tonegawa, S. (2017). Engrams and circuits crucial for systems consolidation of a
646   memory. Science *356*, 73–78.

647 Köhler, C. (1985). A projection from the deep layers of the entorhinal area to the
648 hippocampal formation in the rat brain. Neurosci. Lett. *56*, 13–19.

649 Koster, R., Chadwick, M.J., Chen, Y., Berron, D., Banino, A., Düzel, E., Hassabis, D., and
650 Kumaran, D. (2018). Big-Loop Recurrence within the Hippocampal System Supports
651 Integration of Information across Episodes. Neuron *99*, 1342–1354.e6.

652 Kumaran, D., Hassabis, D., and McClelland, J.L. (2016). What Learning Systems do
653 Intelligent Agents Need? Complementary Learning Systems Theory Updated. Trends Cogn.
654 Sci. *20*, 512–534.

655 Marr, D. (1971). Simple memory: a theory for archicortex. Philos. Trans. R. Soc. Lond. B
656 Biol. Sci. *262*, 23–81.

657 McClelland, J.L., McNaughton, B.L., and O'Reilly, R.C. (1995). Why there are
658 complementary learning systems in the hippocampus and neocortex: insights from the
659 successes and failures of connectionist models of learning and memory. Psychol. Rev. *102*,
660 419.

661 McClure, C., Cole, K.L.H., Wulff, P., Klugmann, M., and Murray, A.J. (2011). Production and
662 titering of recombinant adeno-associated viral vectors. J. Vis. Exp. e3348.

663 Murray, A.J., Sauer, J.-F., Riedel, G., McClure, C., Ansel, L., Cheyne, L., Bartos, M.,
664 Wisden, W., and Wulff, P. (2011). Parvalbumin-positive CA1 interneurons are required for
665 spatial working but not for reference memory. Nat. Neurosci. *14*, 297–299.

666 Naber, P.A., Lopes da Silva, F.H., and Witter, M.P. (2001). Reciprocal connections between
667 the entorhinal cortex and hippocampal fields CA1 and the subiculum are in register with the
668 projections from CA1 to the subiculum. Hippocampus *11*, 99–104.

669 Ognjanovski, N., Schaeffer, S., Wu, J., Mofakham, S., Maruyama, D., Zochowski, M., and
670 Aton, S.J. (2017). Parvalbumin-expressing interneurons coordinate hippocampal network
671 dynamics required for memory consolidation. Nat. Commun. *8*, 15039.

672 Pastoll, H., White, M., and Nolan, M. (2012). Preparation of parasagittal slices for the
673 investigation of dorsal-ventral organization of the rodent medial entorhinal cortex. J. Vis.
674 Exp.

675 Petreanu, L., Huber, D., Sobczyk, A., and Svoboda, K. (2007). Channelrhodopsin-2–assisted
676 circuit mapping of long-range callosal projections. Nat. Neurosci. *10*, 663–668.

677 Rozov, A., Rannap, M., Lorenz, F., Nasretdinov, A., Draguhn, A., and Egorov, A.V. (2020).
678 Processing of Hippocampal Network Activity in the Receiver Network of the Medial
679 Entorhinal Cortex Layer V. The Journal of Neuroscience *40*, 8413–8425.

680 Ruth, R. E., Collier, T. J. & Routtenberg, A. Topography between the entorhinal cortex and
681 the dentate septotemporal axis in rats: I. Medial and intermediate entorhinal projecting cells.
682 J. Comp. Neurol. **209**, 69–78 (1982).
683
684 Schapiro, A.C., Turk-Browne, N.B., Botvinick, M.M., and Norman, K.A. (2017).
685 Complementary learning systems within the hippocampus: a neural network modelling
686 approach to reconciling episodic memory with statistical learning. Philos. Trans. R. Soc.
687 Lond. B Biol. Sci. *372*.

688 Sürmeli, G., Marcu, D.C., McClure, C., Garden, D.L.F., Pastoll, H., and Nolan, M.F. (2015).
689 Molecularly Defined Circuitry Reveals Input-Output Segregation in Deep Layers of the
690 Medial Entorhinal Cortex. Neuron *88*, 1040–1053.

691 Squire, L. R., Genzel, L., Wixted, J. T. & Morris, R. G. Memory consolidation. Cold Spring
692 Harb. Perspect. Biol. **7**, a021766 (2015).
693
694 Swanson, L.W., and Köhler, C. (1986). Anatomical evidence for direct projections from the
695 entorhinal area to the entire cortical mantle in the rat. J. Neurosci. *6*, 3010–3023.

696 Tamamaki, N., and Nojyo, Y. (1995). Preservation of topography in the connections between
697 the subiculum, field CA1, and the entorhinal cortex in rats. J. Comp. Neurol. *353*, 379–390.

698 Wang, Y., Kakizaki, T., Sakagami, H., Saito, K., Ebihara, S., Kato, M., Hirabayashi, M.,
699 Saito, Y., Furuya, N., and Yanagawa, Y. (2009). Fluorescent labeling of both GABAergic and
700 glycinergic neurons in vesicular GABA transporter (VGAT)–Venus transgenic mouse.
701 Neuroscience *164*, 1031–1043.

702 Witter, M.P., and Amaral, D.G. (1991). Entorhinal cortex of the monkey: V. Projections to the
703 dentate gyrus, hippocampus, and subicular complex. J. Comp. Neurol. *307*, 437–459.

704 Witter, M.P., Doan, T.P., Jacobsen, B., Nilssen, E.S., and Ohara, S. (2017). Architecture of
705 the Entorhinal Cortex A Review of Entorhinal Anatomy in Rodents with Some Comparative
706 Notes. Front. Syst. Neurosci. *11*, 46.

707 Wozny, C., Beed, P., Nitzan, N., Pössnecker, Y., Rost, B.R., and Schmitz, D. (2018).
708 VGLUT2 Functions as a Differential Marker for Hippocampal Output Neurons. Front. Cell.
709 Neurosci. *12*, 337.

710

711

712
713

714

715

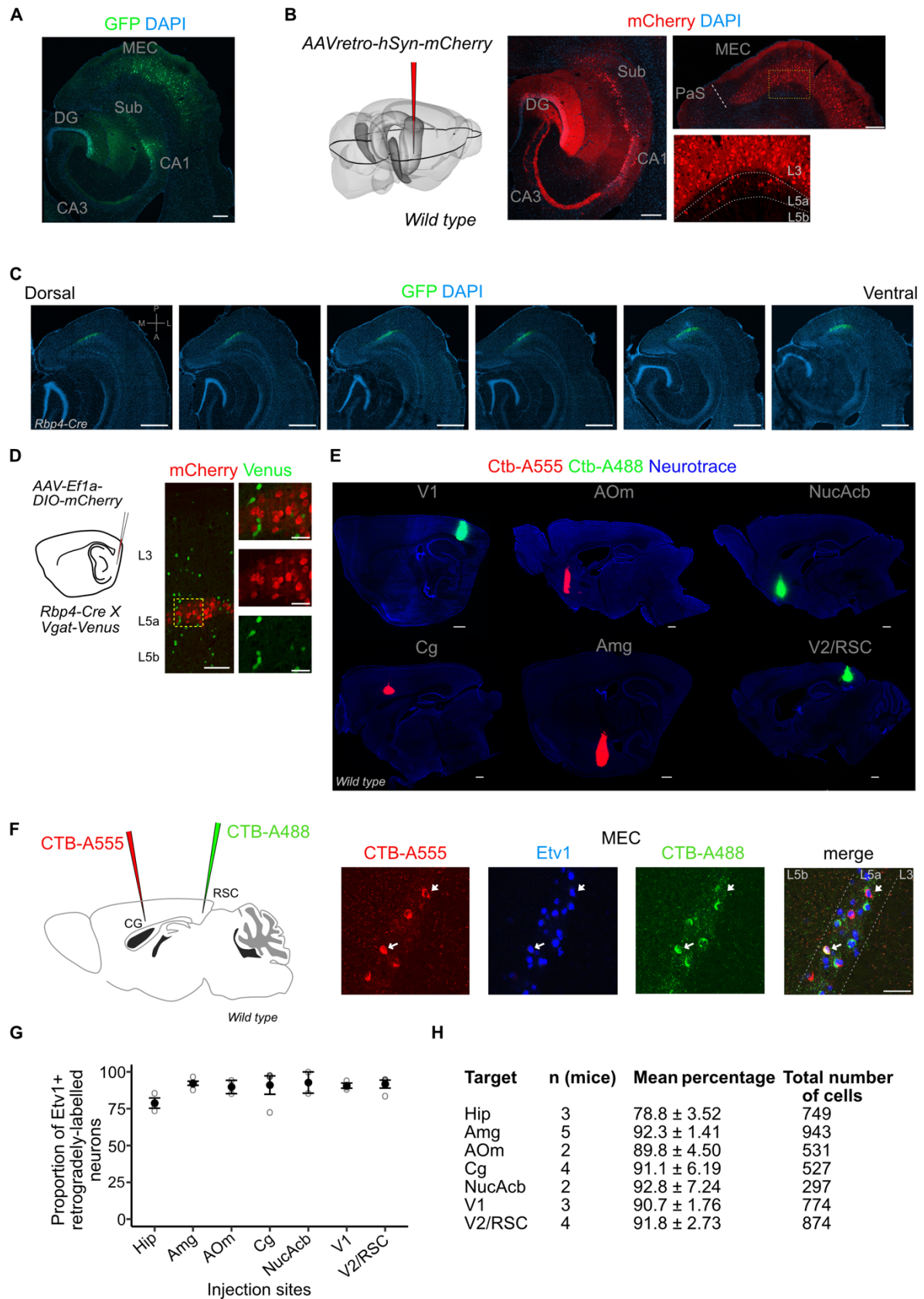716

717

718

719

720

721

722

723

Figure supplements

Target	n (mice)	Mean percentage	Total number of cells
Hip	3	78.8 ± 3.52	749
Amg	5	92.3 ± 1.41	943
AOm	2	89.8 ± 4.50	531
Cg	4	91.1 ± 6.19	527
NucAcb	2	92.8 ± 7.24	297
V1	3	90.7 ± 1.76	774
V2/RSC	4	91.8 ± 2.73	874

Figure 1, figure supplement 1. Injection site images, quantification of co-localisation between retrograde markers and Etv1.

A, Immunostained horizontal sections showing the injection site in the intermediate hippocampus of a retrograde AAV virus. L3 and L5a cells in the MEC were retrogradely-labelled via GFP expression driven by the CAG (CMV early enhancer/chicken β actin) promoter (Scale bar: 200 μm).
B, Results in (A) were replicated with an AAV virus that enables retrograde labelling of cells via expression of mCherry driven by the human synapsin (hSyn) promoter (Scale bar: 200 μm).
C, Immunostained brain sections in horizontal plane from a single brain showing the dorso-ventral spread of virus-mediated reporter gene expression in the Rbp4-Cre mice (Scale bar: 500 μm).
D, Schemmatic of a Cre-dependent mCherry expressing virus injection in the deep MEC of Rbp4-Cre X Vgat-Venus mouse line (left). Immunostained brain sections in the MEC showing absence of overlap between mCherry and Venus which marks GABAergic interneurons (right). Scale bar: 100 μm, Inset scale bar: 30 μm)
E, Immunostained brain sections in the sagittal plane showing injection sites of fluorophore-coupled CTB (Cholera toxin beta subunit; Scale bar: 500 μm).
F, Schematic of a two-colour retrograde dye injection in the cingulate and retrosplenial cortices of wild-type mice (left). Immunostaining in the MEC shows overlap between Etv1 expression and retrograde dyes (right; Scale bar: 50 μm)
G,H, Quantification of overlap between retrograde labelling from cortical target areas and Etv1 expression in L5a of the MEC. The number of mice, mean proportion and total cells counted for each area are shown in the table.

Hip, hippocampus; Amg, amygdala; AOm, medial anterior olfactory area; Cg, cingulate area; NucAcb, nucleus accumbens; V1, primary visual cortex; V2, secondary visual areas; RSC, retrosplenial cortex.
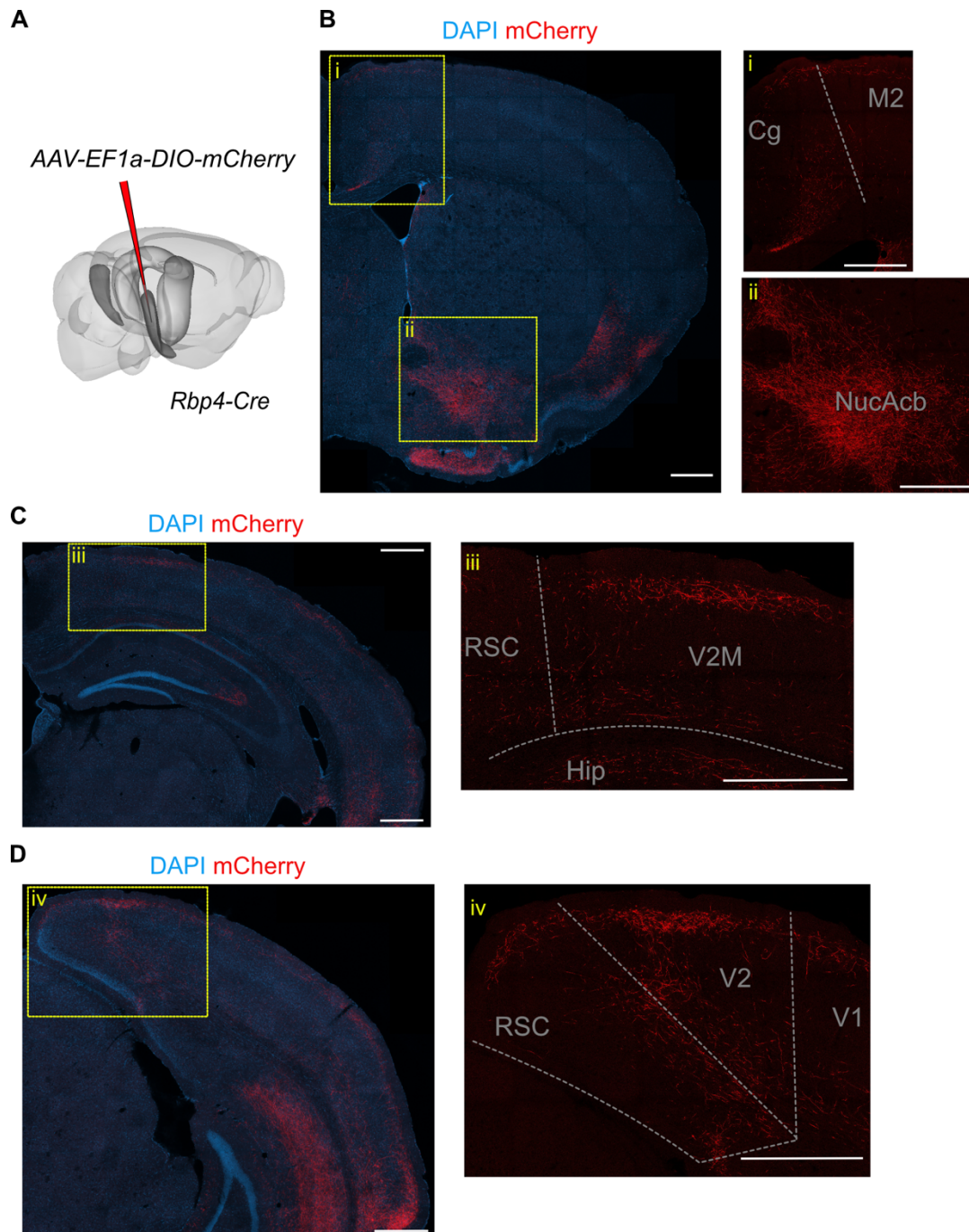
Figure 1, figure supplement 2. L5a neurons of the MEC innervate neocortical and subcortical areas.
A. Schematic showing the injection site of a Cre-dependent virus in the deep MEC of *Rbp4-Cre* mice.
B. Confocal image of a coronal brain slice showing axons originating from entorhinal L5a in the anterior telencephalon. Insets show higher magnification images of boxed areas.
C. Confocal image of a coronal brain slice showing axons originating from entorhinal L5a in the mid-telencephalon. Inset shows higher magnification image of boxed area.
D. Confocal image of a coronal brain slice showing axons originating from entorhinal L5a in the posterior telencephalon. Inset shows higher magnification image of boxed area.

Cg, cingulate area; M2, secondary motor area; V1, primary visual cortex; V2M, secondary visual area (medial); RSC, retrosplenial cortex; RSC, retrosplenial cortex; Hip, hippocampus; NucAcb, nucleus accumbens.
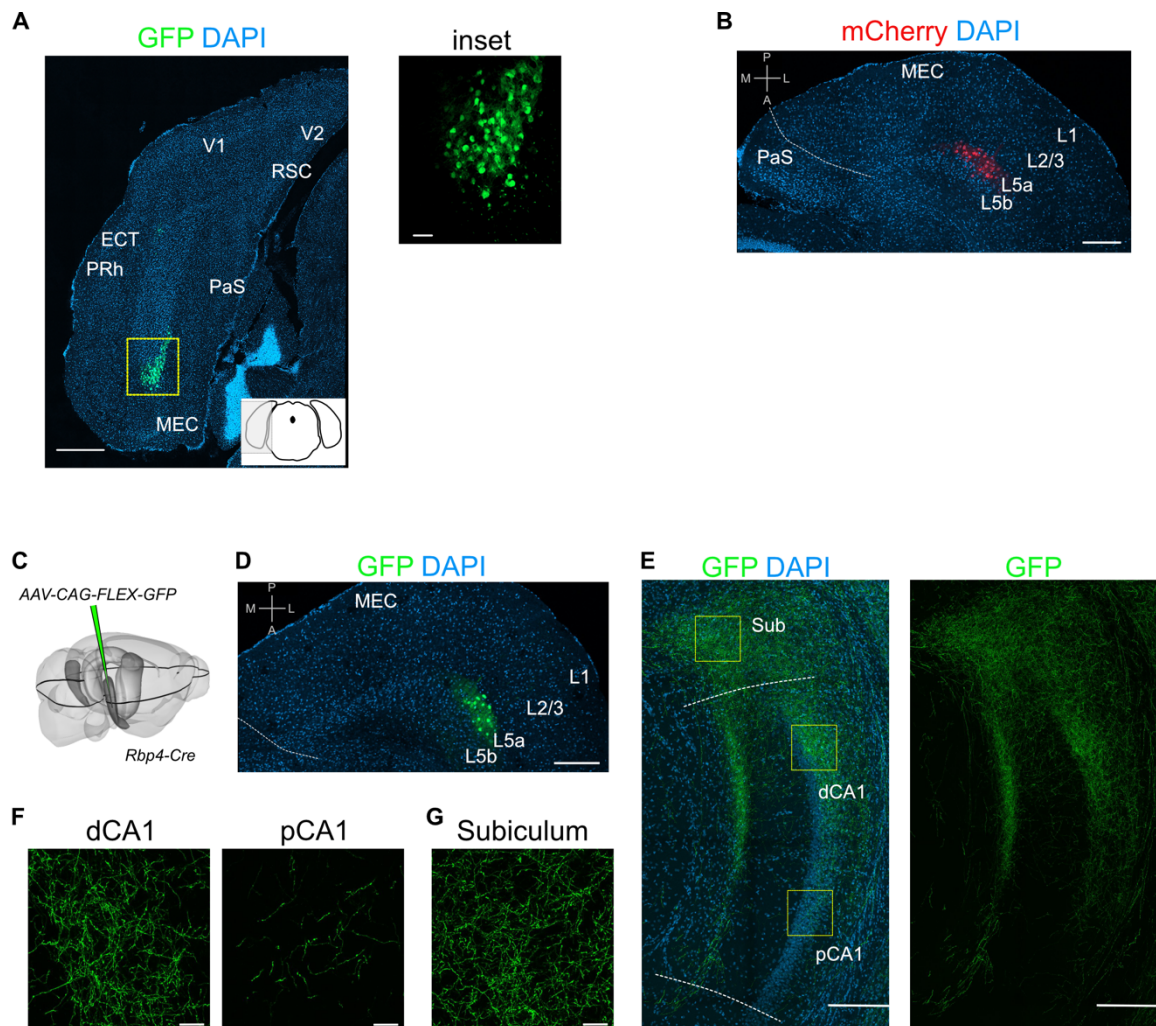
Figure 2, figure supplement 1. Injection site images and additional examples of axon labelling in CA1.

A, Immunostained brain section in the coronal plane showing cell body labelling at the injection site in MEC (Scale bar: 500 µm). Inset shows a higher magnification view of the boxed area (Scale bar: 50 µm). Schematic of a coronal brain section indicates the antero-posterior position of the section.

B, Immunostained brain section in the horizontal plane showing cell body labelling at the injection site in MEC (Scale bar: 200 µm).

C, Schematic showing the injection site of a Cre-dependent virus in the deep MEC of *Rbp4-Cre* mice. The black outline in the horizontal plane roughly corresponds to the dorso-ventral position of the slice shown in (D).

D, Immunostained brain section in the horizontal plane showing cell body labelling at the injection site in MEC (Scale bar: 200 µm).

E, Immunostained brain section in the horizontal plane showing the distribution of axons of MEC L5a cells in the subiculum (Sub), distal CA1 (dCA1) and proximal CA1 (pCA1) (Scale bar: 200 µm).

F, High-magnification images of the pyramidal cell layer in dCA1 and pCA1 showing axonal and synaptic labelling (Scale bar: 20 µm).

G, High-magnification image of the subiculum showing axonal labelling (Scale bar: 20 µm).

Prh, Perirhinal cortex; ECT, Ectorhinal cortex; V1, primary visual cortex; V2, secondary visual cortex; RSC, retrosplenial cortex; PaS, parasubiculum.
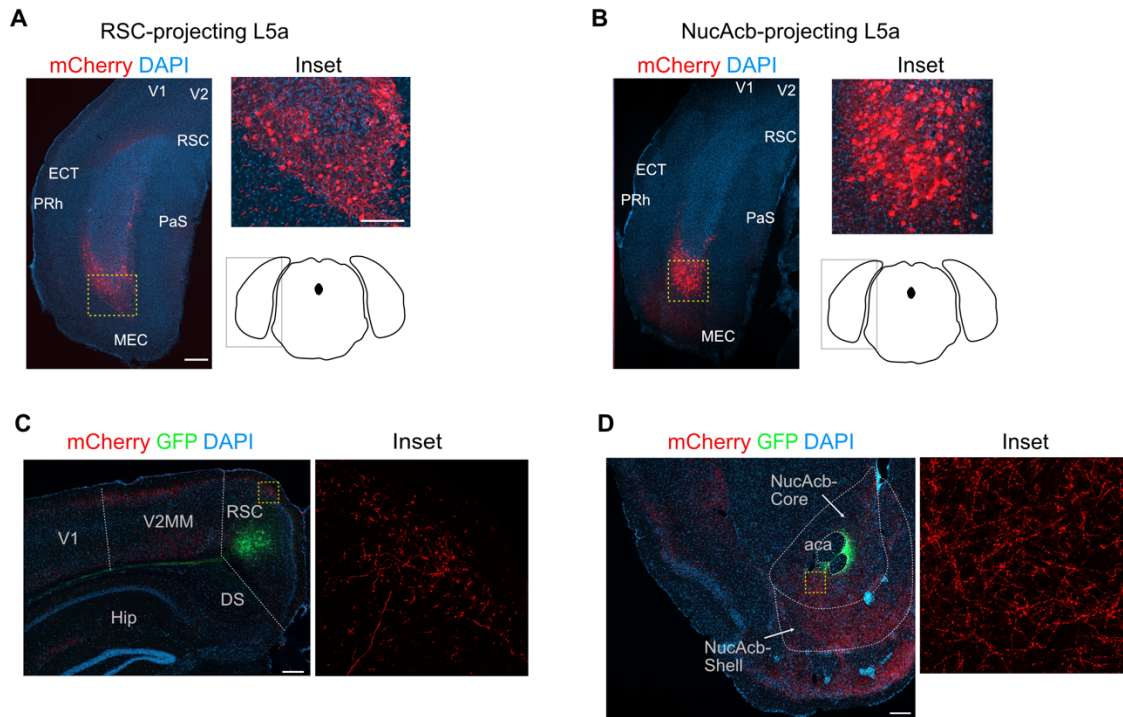
Figure 3, figure supplement 1. Combinatorial viral strategy effectively labels L5a cells of the MEC and their cortical projections.

A, B, Coronal brain sections showing labelled neurons in MEC with the combinatorial viral strategy (Scale bar: 500 μm). Inset: high-magnification confocal image of boxed region in left panel showing cell bodies in MEC expressing mCherry. Schematic of a coronal brain section indicates the antero-posterior position of the sections.

C, D, Coronal brain sections showing GFP expression and mCherry-labelled axon terminals at the injection sites in retrosplenial cortex (**D**) and nucleus accumbens (**E**) (Scale bar: 500 μm). Inset: high-magnification of boxed region in left panel.

RSC, retrosplenial cortex; NucAcb, nucleus accumbens; DS, dorsal subiculum; aca, anterior commissure anterior part; V2, secondary visual area medial part
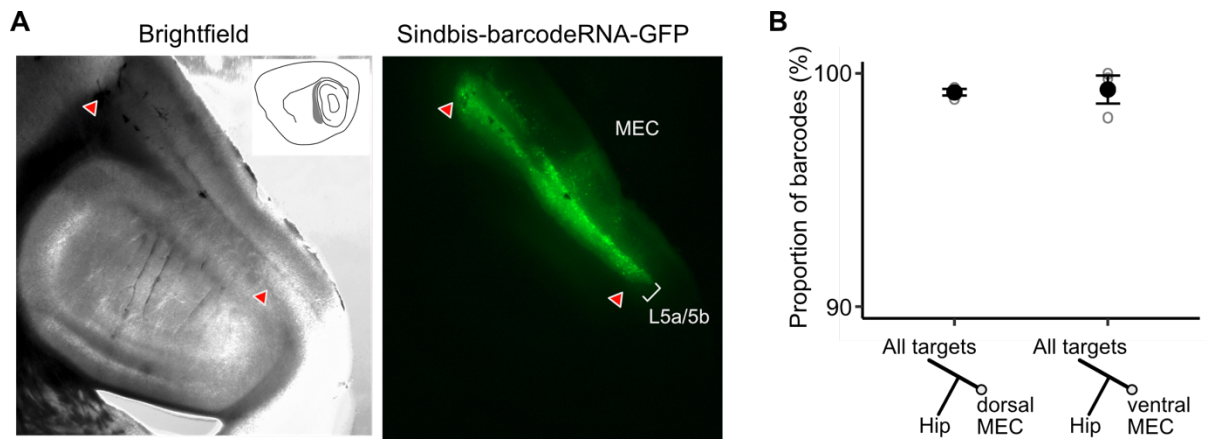
Figure 4, figure supplement 1. Verification of viral expression and further MAPseq data visualisation.
A, Brightfield and epifluorescence microscope images of the injection site on a sagittal brain section showing the spread of neurons infected by the MAPseq virus library in wild type mice.
B, A neuron's position in the dorso-ventral axis does not affect the likelihood of collateralisation of its axons to the hippocampus (Paired two-tailed Wilcoxon signed rank test, p = 0.75, median proportion of collateralizing barcodes in dEC = 98.4%, vEC = 98.9%, n = 3).

A

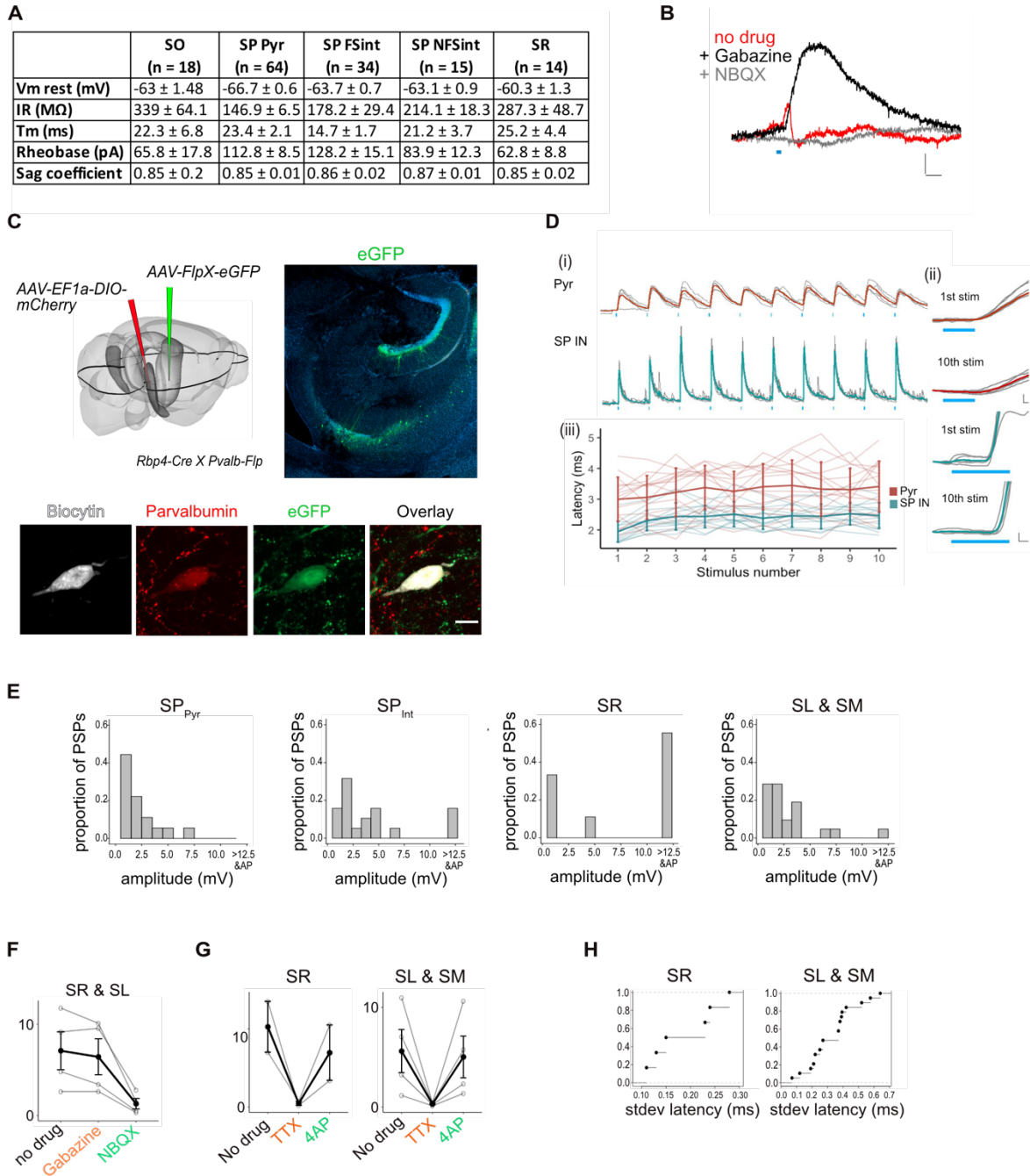|	SO (n = 18)	SP Pyr (n = 64)	SP FSint (n = 34)	SP NFSint (n = 15)	SR (n = 14)
Vm rest (mV)	-63 ± 1.48	-66.7 ± 0.6	-63.7 ± 0.7	-63.1 ± 0.9	-60.3 ± 1.3
IR (MΩ)	339 ± 64.1	146.9 ± 6.5	178.2 ± 29.4	214.1 ± 18.3	287.3 ± 48.7
Tm (ms)	22.3 ± 6.8	23.4 ± 2.1	14.7 ± 1.7	21.2 ± 3.7	25.2 ± 4.4
Rheobase (pA)	65.8 ± 17.8	112.8 ± 8.5	128.2 ± 15.1	83.9 ± 12.3	62.8 ± 8.8
Sag coefficient	0.85 ± 0.2	0.85 ± 0.01	0.86 ± 0.02	0.87 ± 0.01	0.85 ± 0.02

B

C

D

E

F

G

H

Figure 5, figure supplement 1. Experimental design and properties of responses to optogenetic stimulation of axons originating from L5a of the MEC.

A, Summary table for biophysical properties of neurons recorded in the study.

B, An example of a biphasic response recorded from a pyramidal neuron upon 3ms stimulation of axons of MEC L5a neurons in CA1. A late hyperpolarising (red) response was abolished by application of Gabazine to reveal a larger depolarising PSP (black) which was abolished by application of NBQX (grey) (Scale bar: 10 ms, 0.5 mV).

C, Experimental strategy for fluorescence guided patch-clamp recordings made from Parvalbumin expressing neurons. Left: A FlpX-dependent GFP expressing virus was injected in the hippocampus in *Rbp4-CreX Pvalb-Flp* mice. Right: Confocal image of horizontal slice showing labelled interneurons in the hippocampus. Bottom: An example fast-spiking interneuron marked as described in **c**, that showed depolarising PSP upon light stimulation. During recording, the neuron was filled with biocytin and later stained with Streptavidin and Anti-Parvalbumin antibody.

D, (i) Traces of responses to a train of 10 light stimulation (blue lines), showing relatively stable EPSP amplitude across simulations. (Scale bar: 30 ms, 1 mV) (ii) Magnified images of 1st and 10th pulse illustrate the invariant latency in one example cell (Scale bars: 0.5 ms, 0.5 mV) (iii) Quantification of latency across the train in all cells. Error bars represent SEM.

E, Plots showing the frequency distribution of PSP amplitudes in pyramidal neurons and interneurons. PSPs over 12.5 mV were detected in interneurons and often resulted in spiking responses. (SP_{Pyr} : n = 19, SP_{int} : n = 19, SR : n = 9, SL&SM : n = 22 cells).

F, Effects of bath application of Gabazine and NBQX on PSPs recorded from interneurons in SR and SL. The PSP amplitudes were largely unaffected by application of Gabazine (SR: n = 2 cells & SL n = 2 cells, p = 0.28, 2-tailed Student's t test) but were largely blocked by NBQX (SR: n = 2 cells & SL n = 2 cells, p = 0.04, 2-tailed Student's t test) indicating AMPA receptor mediated glutamatergic synaptic transmission.

G, Effects of bath application of TTX and 4-AP on the response amplitude PSPs recorded from interneurons in SR, SL and SM (SR: n = 2, SL: n = 3, SM: n = 1 cells).

H, Cumulative probability plots of standard deviation of latencies for neurons with PSP responses that were > 1 mV in amplitude. EPSPs of interneurons in all layers except SO had a short latency after light stimulation (mean latency SR: 2.00 ± 0.08 ms, n = 6 cells; SL & SM: 2.12 ± 0.21 ms, n = 23 cells). In SO 2 out of 3 of the evoked PSPs had a larger latency of onset (mean latency = 8.5 ± 0.63 ms, n = 2 cells, 2 mice, data not shown).